

Probing fermionic asymmetric dark matter cores using global neutron star properties

Nathan Rutherford,^{1,*} Chanda Prescod-Weinstein,^{1,†} and Anna Watts^{2,‡}

¹*Department of Physics and Astronomy, University of New Hampshire, Durham, New Hampshire 03824, USA*

²*Anton Pannekoek Institute for Astronomy, University of Amsterdam, Science Park 904, 1098XH Amsterdam, The Netherlands*

It is possible for asymmetric dark matter (ADM) to accumulate in neutron star interiors and affect their global properties. Considering the effects of this accumulation, neutron star mass-radius measurements can deliver new insights into the cold dense matter equation of state (EoS). In this paper, we employ Bayesian parameter estimation using real and synthetic neutron star mass-radius data to infer constraints on the combined baryonic matter and fermionic ADM EoS, where the fermionic ADM forms a core in the neutron star interior. Using currently available mass-radius data, we find that the lower bound of the ratio between ADM effective self-repulsion strength (g_χ/m_ϕ) and particle mass (m_χ) can be constrained at the 68% (95%) credible level to $10^{-6.59}$ ($10^{-7.36}$). We also find that, if neutron star mass-radius measurement uncertainties are reduced to the 2% level, the constraints on lower bound on the ratio of g_χ/m_ϕ to m_χ can be improved to $10^{-6.5}$ and $10^{-7.29}$ at the 68% and 95% credible levels, respectively. However, all other combinations, of m_χ , g_χ , and the ADM mass-fraction, F_χ , (i.e., the ratio of the gravitational ADM mass to the gravitational mass of the neutron star) are unconstrained. Furthermore, in the pressure-energy density and mass-radius planes, the inferences which include the possibility of fermionic ADM cores are nearly identical with the inferences that neglect fermionic ADM for $F_\chi \leq 1.7\%$ and neutron star mass-radius uncertainties $\geq 2\%$. Therefore, we find that neutron star mass-radius measurements can constrain ADM in some scenarios and that the presence of ADM in neutron star cores is as equally consistent with current data as the absence of ADM.

I. INTRODUCTION

The extremely compact nature of neutron stars provides a unique environment to probe the behavior of matter at supranuclear densities. Theoretical models of neutron star interiors predict many different types of baryonic matter, such as neutron-rich matter, nuclear pasta, hyperons, and deconfined quarks [1–7]. The microphysics of these hypothetical forms of matter are encoded by the equation of state (EoS), which describes the relation between the pressure and energy density maintained throughout the star. The dense matter EoS can be determined from knowing the gravitational masses and radii of neutron stars. In particular, each EoS can be mapped to a unique mass-radius relation, i.e., the numerical expression that relates all possible, stable neutron star mass and radii, through the Tolman-Oppenheimer-Volkoff equations [8]. Thus, measurements of neutron stars can be used to characterize the mass-radius curve, and thus constrain each hypothetical dense matter EoS.

Analysing the X-ray pulse profile (a rotationally phase and energy-resolved X-ray count spectrum) can be used to infer the masses and radii of neutron stars through the Pulse Profile Modelling (PPM) technique. PPM is a relativistic ray tracing technique that can be used to extract valuable information encoded in the pulse profile, such as mass, radius, and hot spot geometry [for more details on PPM see 9–11]. So far, data from the NASA’s

Neutron Star Interior Composition Explorer (NICER) [12], informed where possible by mass priors from pulsar timing, has been used to infer the masses and radii of three millisecond pulsars using the PPM technique: PSR J0740+6620 [13–17], PSR J0030+0451 [18–20], and most recently, PSR J0437–4715 [21, 22]. The mass-radius measurements of these pulsars have been used in many analyses to set constraints on the dense matter EoS [see e.g., 15, 19, 23–33]. Most recently, [32] has shown that the inferences with the newest mass-radius results from *NICER* improve the reliability of our understanding on the neutron star EoS via the updated chiral effective field theory (χ EFT) calculations of [34] and the degree in which the results are data-driven. However, the uncertainty of the cold dense matter EoS remains.

In the near future, improved mass-radius constraints on targets already analyzed by *NICER* are expected. Additionally, the mass-radius measurements of four more sources are anticipated. During the next decade, large area X-ray spectral-timing missions are anticipated to perform PPM on more neutron stars with improved uncertainties. Such missions include the Chinese mission concept *eXTP* (the enhanced X-ray Timing and Polarimetry mission, [35]), the NASA probe-class mission concept *STROBE-X* (the Spectroscopic Time-Resolving Observatory for Broadband Energy X-rays, [36]), and the ESA’s L-class mission *Athena* (Advanced Telescope for High ENergy Astrophysics, [37]).y, many of the EoS studies that consider PPM derived mass-radius measurements only account for the presence of baryonic matter and its potential phase transitions. However, there is a growing understanding that dark matter may form part of neutron star structures and therefore affect the ob-

* Corresponding author: nathan.rutherford@unh.edu

† chanda.prescod-weinstein@unh.edu

‡ A.L.Watts@uva.nl

servable properties of neutron stars. To fully assess the range of neutron star EoS, we must therefore also study the inclusion of a dark matter component in our models. Dark matter can occupy two spatial regimes: a dark matter halo that extends through and beyond the baryonic radius of the neutron star, and a dark matter core inside the neutron star’s interior. Dark matter halos around neutron stars have been shown to increase the gravitational masses and tidal deformabilities of the stars when compared to a neutron star with no ADM with an identical central baryonic energy density, if the dark matter mass distribution is mostly beyond the baryonic surface [38–44]. However, if most of the dark matter halo distribution resides within the baryonic radii of neutron stars, halos can reduce the gravitational masses and radii of these stars [see e.g., 45]. In addition, the presence of any dark matter halo can significantly impact the exterior space-time around neutron stars, which would alter the interpretation of *NICER*’s mass-radius measurements [45–47]. Interestingly, dark matter halos could possibly form stable ultra-compact neutron stars with compactness greater than $1/3$, which could serve as a black hole mimic [48]. If dark matter forms a core inside neutron star interiors, the gravitational masses, radii, and tidal deformabilities have been shown to decrease when compared to their purely baryonic counterparts with the same central baryonic energy density [49–56]. Therefore, it is evident that, because dark matter can affect the measurable properties of neutron stars, the possible presence of it must be accounted for in analyses of the neutron star mass-radius measurements and the EoS.

There are a variety of proposed methods to constrain the presence of dark matter in and around neutron stars. For instance, by considering one or multiple representative baryonic EoSs, constraints on the dark matter particle mass, mediator mass, and mass-fraction can be made using gravitational wave and neutron star mass-radius measurements [43, 46, 52, 53, 57–71]. More specifically, using one or more baryonic EoSs allows for constraints on the dark matter mass-fraction as a function of particle mass [43, 52, 53, 61, 62], the dark matter Fermi momentum and particle mass [57, 71], several dark matter parameters by imposing hard cut-offs on the maximum neutron star mass and tidal deformability of a $1.4 M_{\odot}$ neutron star [59, 60, 67–69], correlations between dark matter and baryonic matter parameters [63–66, 70], and Bayesian inferences to estimate the dark matter parameter space [46, 58]. Analytical calculations of the maximum accumulated dark matter mass before gravitational collapse to a black hole inside a neutron star can be used to tightly constrain dark matter models through observations of old neutron stars [72–75]. When an additional dark matter component is considered in simulations of binary neutron star mergers it has been shown that dark matter can leave detectable signatures on the gravitational wave and electromagnetic counterparts, which can constrain the dark matter particle mass and the total accumulated dark matter mass [76–78]. Finally, due to

their extremely compact natures, neutron stars can efficiently capture dark matter within their interiors and thus can provide constraints on the dark matter–nucleon cross section and particle mass [79].

In our previous work [80], we investigated constraints on bosonic asymmetric dark matter (ADM) cores inside neutron stars by performing a full Bayesian inference in which all parameters in the neutron star EoS model are allowed to vary. We assumed the dark matter was 100% comprised of the self-repulsive bosonic ADM of [38]. The main motivation of the ADM paradigm suggests that the cosmic history between dark matter and baryonic is strongly tied together given that the observed dark matter mass density in the universe is only five times greater than that of baryonic matter. That is, similar to the baryon asymmetry in the early universe, dark matter also had an asymmetry between it and anti-dark matter, which produced the relic abundance of dark matter observed today in the universe [81, 82]. A “dark asymmetry” between dark matter and anti-dark matter in the early universe would allow for small attractive interactions with baryonic matter and substantial repulsive self-interactions.

By combining the EoS of the [38] bosonic ADM model with the parametrized piecewise polytropic (PP) model of [1] and restricting the study to simulated neutron star mass-radius measurements with and without bosonic ADM cores, in [80] we explored the possible inferred constraints on both of the bosonic ADM and baryonic EoSs. From these inferences, we found that the uncertainties on the baryonic EoS are relaxed when bosonic ADM cores are taken into account. Moreover, in [80] we found that, if the baryonic EoS could be constrained more tightly, constraints on the ADM mass-fraction and the ratio of the effective bosonic ADM self-repulsion strength to the particle mass can be made. Lastly, we concluded that the ADM particle mass and self-repulsion cannot be individually constrained using neutron star mass-radius measurements.

Here, we expand on our work in [80] by taking into account fermionic ADM cores, and considering both real and synthetic PPM derived mass-radius data. Modeling the dark matter core as fermionic ADM instead of bosonic ADM is physically interesting because fermionic ADM cores have additional support against gravity through the Fermi degeneracy pressure, thus expanding the allowed ADM parameter space to be studied because the self-repulsion is allowed to be zero. We additionally consider real data for this work because [56] showed that the presence of ADM cores does not modify the universal relations used to model the oblateness of neutron stars.¹ By utilizing both real and synthetic neutron mass-radius data, we can investigate current and potential future constraints on fermionic ADM cores.

¹ For further details on the universal oblateness relations of neutron stars see [83, 84].

In this work, we assume the fermionic ADM cores are described by the [38] model and neglect the possibility of ADM halo configurations, because the existence of any halo will alter the exterior space-time and thus modify how PPM is performed. This work will consider the mass-radius measurements of PSR J0740+6620 [14] and PSR J0030+0451 [18]. There have been several updates to PSR J0740+6620 [16, 17] and PSR J0030+0451 [20], as well as a new mass-radius measurement for PSR J0437–4715 [21], which was released during the completion of this work. However, we still consider the mass-radius posteriors of PSR J0030+0451 [18] and PSR J0740+6620 [14] for two key reasons: the first is so that this work is fully comparable to our previous work on bosonic ADM [80] and the other is because our synthetic scenario best demonstrates what can be achieved with tighter mass-radius uncertainties.

For the simulated neutron star data, we consider six possible *STROBE-X* sources because *STROBE-X* mission is expected to provide lower uncertainties than *NICER* [36, 85]. We call this scenario, *Future-X*, after the original *Future-X* scenario in our previous work. By incorporating fermionic ADM with both real and synthetic data into our Bayesian framework, this work aims to quantify the possible constraints on the fermionic ADM EoS for current missions and future missions, namely *NICER* and *STROBE-X*. Furthermore, the other objective is to determine the effects of including fermionic ADM on the neutron star pressure-energy density and mass-radius posteriors.

The work presented in this manuscript shows that the current *NICER* and future *STROBE-X* measurements are able to place constraints on the lower bound of the ratio between the ADM particle mass and effective self-repulsion strength. However, under the current uncertainties of the baryonic EoS, neither *NICER* nor *STROBE-X* can constrain the fermionic ADM particle mass, effective self-repulsion strength, or mass-fraction. Finally, we find that the mass-radius ADM admixed neutron star posteriors are fully consistent with their neglecting ADM posterior counterparts.

This paper is organized as follows. In Sec. II, we motivate the two-fluid TOV equations and describe the baryonic matter and fermionic ADM EoSs. Sec. III discusses our Bayesian inference framework for providing constraints on the ADM admixed neutron star EoS, the baryonic matter EoS priors, the constraints on the fermionic ADM EoS parameter space, and the selected neutron star mass-radius measurements. In Sec. IV, we study the inferences for both the *NICER* data and *Future-X* scenario. Finally, in Sec. V, we discuss our results. Throughout this work, we use the *diag*(−, +, +, +).

II. MODELING THE STRUCTURE OF ADM ADMIXED NEUTRON STARS

Traditionally, the mass-radius relation of neutron stars is computed by iteratively solving the Tolman-Oppenheimer-Volkoff (TOV) equations [86, 87] for a given baryonic matter equation of state and range of central energy densities [8]. However, to compute the mass-radius relation of neutron stars with ADM, the single fluid mass-radius relation calculation must be modified. In this section, we describe how to model the structure of ADM admixed neutron stars using the two-fluid formalism, and describe the baryonic matter and ADM equations of state used in our analysis. The combination of the baryonic matter EoS, ADM EoS, and two-fluid formalism, allow for the ADM admixed neutron star mass-radius relation to be computed.

A. The two-fluid formalism

The global properties, such as mass and radius, of an ADM admixed neutron star can be computed by adopting the two-fluid formalism, which assumes that the interactions between the Standard Model and ADM are solely gravitational [see e.g., 45, 47, 49, 53, 56, 61, 77, 88, 89]. The two-fluid formalism is an appropriate framework to study ADM admixed neutron stars because any non-gravitational interfluid interaction between ADM and the Standard Model is expected to be negligible [90, 91]. The assumption that ADM and baryonic matter interact only gravitationally implies that ADM and baryonic matter satisfy their own conservation of energy-momentum equation. Thus, both ADM and baryonic matter can be treated as two distinct fluids, which can be expressed in terms of pressure and energy density as

$$p(r) = p_B(r) + p_\chi(r) \quad (1)$$

$$\epsilon(r) = \epsilon_B(r) + \epsilon_\chi(r), \quad (2)$$

where p_B (ϵ_B) is the baryonic matter pressure (energy density) as a function of radius r and p_χ (ϵ_χ) is the ADM pressure (energy density) as function of r . The substitution of Eqs. 1 and 2 into the single-fluid TOV equations yields the two-fluid TOV equations:

$$\frac{dp_B}{dr} = -(\epsilon_B + p_B) \frac{Gc^2 M(r) + 4\pi r^3 Gp(r)}{c^2 r [rc^2 - 2GM(r)]} \quad (3)$$

$$\frac{dp_\chi}{dr} = -(\epsilon_\chi + p_\chi) \frac{Gc^2 M(r) + 4\pi r^3 Gp(r)}{c^2 r [rc^2 - 2GM(r)]} \quad (4)$$

$$\frac{dM_B(r)}{dr} = 4\pi r^2 \frac{\epsilon_B(r)}{c^2} \quad (5)$$

$$\frac{dM_\chi(r)}{dr} = 4\pi r^2 \frac{\epsilon_\chi(r)}{c^2}, \quad (6)$$

where $M_\chi(r)$ is the gravitational mass of ADM, $M_B(r)$ is the gravitational mass of baryonic matter, and $M(r) =$

$M_B(r) + M_\chi(r)$. The two-fluid TOV equations can then be simultaneously solved for the gravitational masses, radii, and pressures of each fluid given their respective equations of state and central energy densities. More specifically, the pressures and gravitational masses of ADM and baryonic matter are solved simultaneously until either one of the fluid pressures reaches zero. The integration is stopped and then resumed using the single-fluid TOV equations with the last pressure value of the remaining fluid as the initial condition. Since the two-fluid TOV equations can be solved to obtain the gravitational masses and radii of both ADM and baryonic matter, they can also be used to numerically compute the ADM admixed mass-radius relation. Similar to how the baryonic matter neutron star mass-radius relation is numerically computed, the ADM admixed neutron star mass-radius relation is obtained by iteratively solving the two-fluid TOV equations for a given EoS and range central energy densities for both ADM and baryonic matter, respectively.

The two-fluid TOV equations allow for a clear distinction between the ADM core radius (R_χ) and the baryonic matter radius (R_B), which makes it possible to define the ADM mass-fraction, F_χ . The mass-fraction is defined as the ratio of the ADM gravitational mass to the total gravitational mass of the ADM admixed neutron star, and it is given by

$$F_\chi = \frac{M_\chi(R_\chi)}{M_\chi(R_\chi) + M_B(R_B)}, \quad (7)$$

where $M_\chi(R_\chi)$ is the total accumulated ADM gravitational mass evaluated at R_χ and $M_B(R_B)$ is the baryonic matter gravitational mass evaluated at R_B . The ADM mass-fraction is useful because the total gravitational mass and radius of an ADM admixed neutron star is strongly dependent on the value of F_χ [see 52, 55, 92]. Moreover, when specific assumptions about the baryonic matter EoS are made, the ADM mass-fraction can be constrained tightly by neutron star measurements [52, 53, 80, 88] and can be used to place constraints on the ADM particle mass [47, 55, 62, 88]. The F_χ is an optimal parameter to consider in our analysis. Finally, to compute the structure of an ADM admixed neutron star for a given F_χ and central baryonic energy density, we follow the numerical algorithm outlined in [80].

B. The baryonic matter and ADM equations of state

In order to model neutron stars that have a baryonic matter and a potential fermionic ADM core component, we need to solve the two-fluid TOV equations. This requires an equation of state for each type of matter. While it is common practice to model the baryonic matter EoS using one or more of the available tabulated EoSs [38, 45, 46, 49–51, 56, 61], we model the baryonic matter EoS using the parametrized piecewise polytropic

(PP) model used in [1, 23–25, 32, 93]. We employ the PP model because it, as well as other polytropic models, can fit many of the tabulated EoS [94]. Moreover, when a wide range of PP EoSs are sampled, the PP model is able to capture the uncertainties in the baryonic EoS due to its parametrized nature. This allows for the PP model to span much of the physically viable space in the mass-radius plane. The parametrized PP model is described by three varying polytropes connected at 2 varying transition densities and considers the calculations of χ EFT at low density. In particular, for densities $\lesssim 0.5n_0$ ($n_0 = 0.16fm^{-3}$) we consider the neutron star crust to be described by the Baym-Pethick-Sutherland (BPS) crust EoS [95], which we then connect to a single polytropic fit of the χ EFT band of [1] between $0.5n_0$ and $1.1n_0$. At densities above $2n_0$, the χ EFT calculations grow increasingly uncertain and eventually break down [96]. Although, χ EFT calculations have been considered up to $1.5 - 2.0n_0$ in other EoS analyses [see e.g., 7, 32, 97], we do not expect the difference in these choices to affect the inferences on the fermionic ADM EoS parameters, as the χ EFT calculations only affect the uncertainties on the baryonic EoS, which is beyond the scope of this work. Additionally, this work seeks to be comparable to our previous work [80]. Thus, for densities $\geq 1.1n_0$, we connect the [1] χ EFT band to the high density piecewise polytropic parameterization. Modeling the baryonic EoS in this way allows us to simultaneously consider the tight constraints delivered by the χ EFT formalism and systematically study the neutron star mass-radius plane [see 1, 94, 98].

Our fermionic ADM core is that of [38], which describes a MeV-GeV mass-scale spin-1/2 ADM particle with repulsive self-interactions mediated by the exchange of an eV-MeV mass-scale vector gauge boson. The ADM vector gauge boson also carries the Standard Model baryon number in order to create the asymmetry between dark matter and anti-dark matter particles in the early universe that is needed to produce the present dark matter mass density of the universe.

The action of the [38] fermionic ADM model in units of $\hbar = c = 1$, is given by

$$S = - \int d^4x \sqrt{-g} [\bar{\chi} (i\gamma_\mu D^\mu + m_\chi) \chi + \frac{1}{2} m_\phi^2 \phi_\mu \phi^\mu + \frac{1}{4} Z_{\mu\nu} Z^{\mu\nu} - g_B \phi_\mu J_B^\mu], \quad (8)$$

where γ_μ are the Dirac matrices that satisfy the anti-commutation relation $\{\gamma_\mu, \gamma_\nu\} = -2g_{\mu\nu}$, g is the determinant of the metric, χ is the charged spin-1/2 Dirac fermionic ADM field, $\bar{\chi} \equiv \chi^\dagger \gamma_0$ is the anti-ADM particle field, $D^\mu = \nabla^\mu + ig_\chi \phi^\mu$ is the $U(1)_{Dark}$ gauge covariant derivative, ∇^μ is the covariant derivative, g_χ is the interacting strength between χ and the vector gauge boson ϕ_μ , m_ϕ is the mass of the ϕ_μ vector field, $Z_{\mu\nu} = \nabla_\mu \phi_\nu - \nabla_\nu \phi_\mu$ is the ϕ_μ field strength tensor, and g_B is the interaction strength of ϕ_μ with the Standard Model baryon current J_B^μ .

We now make two assumptions that make analytic calculations possible and still allow us to gain insight into the system. First, we assume the spacetime to be flat because the deviations of the metric compared to a flat one are negligible on the inverse length scales of neutron stars [52] (for more details see Appendix A). By assuming a flat spacetime, the determinant of the metric in our chosen coordinate system is $g = -r^4 \sin^2(\theta)$. Second, we follow [38] and assume that $g_B \ll g_\chi$, which allows us to ignore the non-gravitational interactions between baryonic matter and ADM, i.e., the $g_B \phi_\mu J_B^\mu$ term in the action. Although robust calculations of this inequality have not been done yet, assuming that $g_B \ll g_\chi$ is physically reasonable because it is expected that $g_\chi \in [10^{-6}, 1]$ for m_ϕ in the eV-MeV mass-scale, which is at least four orders of magnitude greater than the $g_B \leq 10^{-10}$ constraint [38, 91]². Therefore, in order to obey the assumption that $g_B \ll g_\chi$, we approximate the effective self-repulsion strength to a non-zero value that produces ADM cores similar to the physically allowed value of zero in Appendix B.

Given those two assumptions, the equations of motion are

$$[i\gamma_\mu D^\mu + m_\chi] \chi = 0 \quad (9)$$

$$iD^\dagger \bar{\chi} \gamma^\mu - m_\chi \bar{\chi} = 0 \quad (10)$$

$$\nabla_\mu Z^{\mu\nu} + g_\chi \bar{\chi} \gamma^\nu \chi - m_\phi^2 \phi^\nu = 0. \quad (11)$$

By assuming that all of the possible accumulated ADM has thermally equilibrated within the neutron star then the ADM EoS can be computed in the zero temperature limit. Thus, from the equations of motion, we can apply the mean-field approximation to obtain the ADM EoS, which we describe in more detail in Appendix A. With \hbar and c restored, the [38] fermionic ADM EoS is expressed as

$$\begin{aligned} \epsilon_\chi = \frac{c^5 m_\chi^4}{8\pi^2 \hbar^3} & \left[\sqrt{1+z^2} (2z^3+z) - \ln(z + \sqrt{1+z^2}) \right] \\ & + \frac{g_\chi^2}{2m_\phi^2} \frac{c^5 (m_\chi z)^6}{\hbar^3 (3\pi^2)^2} \end{aligned} \quad (12)$$

$$\begin{aligned} p_\chi = \frac{c^5 m_\chi^4}{8\pi^2 \hbar^3} & \left[\sqrt{1+z^2} \left(\frac{2}{3} z^3 - z \right) + \ln(z + \sqrt{1+z^2}) \right] \\ & + \frac{g_\chi^2}{2m_\phi^2} \frac{c^5 (m_\chi z)^6}{\hbar^3 (3\pi^2)^2}, \end{aligned} \quad (13)$$

where ϵ_χ is the fermionic ADM energy density, p_χ is the fermionic ADM pressure, and $z = \hbar k_\chi / m_\chi c$ is the relativity parameter defined in terms of the ADM Fermi

momentum k_χ . By inserting the baryonic matter and fermionic ADM equations of state into the two-fluid TOV equation, the ADM admixed neutron star mass-radius relation can be computed.

III. METHODOLOGY

We will now show how to construct our Bayesian inference framework that considers both baryonic matter and ADM inside neutron star interiors. In this section, we will discuss this inference framework, the prior space of the PP parameterization of the baryonic EoS, constraints on the fermionic ADM EoS parameters, and the source selection for both the real and synthetic data analyses.

A. Bayesian framework

We use the inference framework developed in [80], which adapts the Bayesian analysis of [23–25, 32, 93] to include the possible presence of an ADM EoS. In particular, we use the open source EoS inference code N_{EO}ST v2.0.0, which includes ADM functionality [99]³.

We use Bayes's theorem to write the posterior distribution on all ADM and baryonic equations of state as

$$\begin{aligned} p(\boldsymbol{\theta}, \boldsymbol{\epsilon}_c | \mathbf{d}) & \propto p(\boldsymbol{\theta}) p(\boldsymbol{\epsilon}_c | \boldsymbol{\theta}) p(\mathbf{d} | \boldsymbol{\theta}, \boldsymbol{\epsilon}_c) \\ & \propto p(\boldsymbol{\theta}) p(\boldsymbol{\epsilon}_c | \boldsymbol{\theta}) p(\mathbf{d} | \mathbf{M}(\boldsymbol{\theta}, \boldsymbol{\epsilon}_c), \mathbf{R}(\boldsymbol{\theta}, \boldsymbol{\epsilon}_c)), \end{aligned} \quad (14)$$

where $\boldsymbol{\theta}$ is the vector containing all ADM and baryonic EoS parameters, $\boldsymbol{\epsilon}_c$ is the vector containing the baryonic and ADM central energy densities, \mathbf{d} is the vector containing the masses and radii of the sources from each scenario, $\mathbf{M}(\boldsymbol{\theta}, \boldsymbol{\epsilon}_c)$ is the mass of a produced admixed neutron star, and $\mathbf{R}(\boldsymbol{\theta}, \boldsymbol{\epsilon}_c)$ is the radius of the admixed neutron star. Moreover, by assuming each of the mass-radius datasets are independent of one another and equating the mass-radius datasets to those derived from PPM, we obtain

$$\begin{aligned} p(\boldsymbol{\theta}, \boldsymbol{\epsilon}_c | \mathbf{d}) & \propto p(\boldsymbol{\theta}) p(\boldsymbol{\epsilon}_c | \boldsymbol{\theta}) \\ & \prod_i p(M_i, R_i | d_{PPM,i}), \end{aligned} \quad (15)$$

where i runs over the number of stars for which PPM delivers the mass and radius and $d_{PPM,i}$ is an element in the \mathbf{d} vector in which PPM was used. Furthermore, since the ADM mass-fraction is a function of baryonic and ADM EoS parameters and central energy densities, we can sample over the ADM mass-fraction instead of the ADM central energy density by introducing $F_\chi = F_\chi(\boldsymbol{\theta}, \boldsymbol{\epsilon}_{c,B}, \boldsymbol{\epsilon}_{c,ADM})$. This implies that the posterior distribution $\boldsymbol{\theta}$ and $\boldsymbol{\epsilon}_c$ can be rewritten as

² Note, g_χ is allowed be zero in the [38] fermionic ADM model because the Fermi degeneracy pressure offers the ADM core support against gravitational collapse.

³ <https://github.com/xpsi-group/neost>

$$p(\boldsymbol{\theta}, \boldsymbol{\epsilon}_{c,B}, \mathbf{F}_\chi | \mathbf{d}) \propto p(\boldsymbol{\theta}) p(\boldsymbol{\epsilon}_{c,B} | \boldsymbol{\theta}) p(\mathbf{F}_\chi | \boldsymbol{\theta}, \boldsymbol{\epsilon}_c) \prod_i p(M_i, R_i | d_{PPM,i}), \quad (16)$$

where $\boldsymbol{\epsilon}_{c,B}$ and $\boldsymbol{\epsilon}_{c,ADM}$ are the central energy densities of baryonic matter and ADM, respectively. Sampling over the ADM mass-fraction rather than the ADM central energy density allows for a direct comparison between the potential accumulation methods of ADM in neutron stars and the F_χ prior space.

B. Baryonic matter priors

We will now define the priors on the baryonic matter EoS, which we describe using the parametrized PP EoS model used in [1, 23–25, 32] from Sec. II B. Since the neutron star crust is modeled after the fixed BPS crust EoS [95], the prior ranges that need to be defined are those on the [1] χ EFT band, the three polytropes, and the two varying transition densities between each polytrope. As described in Sec. II B, the [1] χ EFT band is fitted between $0.5n_0$ and $1.1n_0$ using a single polytrope, which is of the form

$$P_{\chi\text{EFT}}(n_B) = K(n_B/n_0)^\Gamma, \quad (17)$$

where $P_{\chi\text{EFT}}$ is the χ EFT pressure as a function of baryonic number density n_B , K is the matching constant to $P_{\chi\text{EFT}}$ in units of MeV fm^{-3} , and Γ is the adiabatic index. Following the fitting procedure in [25], which fits the maximum and minimum pressure bands of a given χ EFT using Eq. 17, the [1] band is well reproduced by $K \in [1.676, 2.814] \text{ MeV fm}^{-3}$ and $\Gamma \in [2.486, 2.571]$. We take the fit parameters for K and Γ to be the prior bounds on the [1] χ EFT band.

In order to produce the three polytropic priors, we consider the allowed ranges described in [93], which define the priors on the first polytropic index (Γ_1), the transition density between the first and second polytrope (n_1), the second polytropic index (Γ_2), the transition density between the second and third polytrope (n_2), and the third polytropic index (Γ_3). The priors on each parameter are given as: $\Gamma_1 \in [1, 4.5]$, $\Gamma_2 \in [0., 8.]$, $\Gamma_3 \in [0.5, 8]$, and $1.5n_0 \leq n_1 < n_2 \leq 8.3n_0$. Here, the transition densities between the three polytropes, n_1 and n_2 , are allowed up to $8.3n_0$ as this is the maximal central density of the PP model [1, 93]. For each PP EoS parameter, we uniformly sample the considered prior ranges.

C. Fermionic ADM priors

We now define the priors on each of the fermionic ADM EoS parameters. In particular, we use the available literature and physical constraints (if any) to construct the

prior spaces on m_χ , F_χ , and g_χ/m_ϕ , all three of which completely define the fermionic ADM EoS.

To define the prior space on the fermionic ADM particle mass, we consider the physical constraints on m_χ from [75, 100]. The considered lower bound on m_χ was obtained by [100], which showed that the minimum m_χ such that no ADM particle can exceed the neutron star escape velocity is

$$m_\chi \geq 10^{-2} \text{ MeV}. \quad (18)$$

On the other hand, [75] considered fermionic ADM core collapse to a black hole inside the host neutron star. The authors showed that in order to avoid the formation of a black hole, regardless of whether the ADM is self-interacting,

$$m_\chi \leq 10^9 \text{ MeV}. \quad (19)$$

Therefore, the prior space on the fermionic ADM particle mass is defined by

$$m_\chi \in [10^{-2} \text{ MeV}, 10^9 \text{ MeV}]. \quad (20)$$

While the prior space on the fermionic ADM particle mass is well constrained, the ADM mass-fraction prior space is not. Typically, the fermionic ADM mass-fraction prior space is defined using physically motivated ADM accumulation methods, such as neutron bremsstrahlung [38, 49], production of ADM in supernovae [38, 92], and neutron conversion to ADM [49, 54, 101]. The neutron Bremsstrahlung reaction of ADM produces the gauge boson ϕ_μ via the conversion of the kinetic energy produced between the scattering of two neutrons (NN), i.e., $NN \rightarrow NN\phi_\mu$. Moreover, since ϕ_μ is strongly coupled to ADM, the reaction of $NN \rightarrow NN\bar{\chi}\chi$ proceeds at a similar rate as that of the neutron Bremsstrahlung reaction. Assuming anti-ADM is repulsed by baryonic matter and ADM is attracted to it, the asymmetry between the energy of ADM and anti-ADM inside the neutron star will preferentially trap ADM and eject the anti-ADM from the star. Since young neutron stars have temperatures around 50 MeV and assuming $m_\chi = 100 \text{ MeV}$, neutron Bremsstrahlung of ADM can produce $\approx 0.02M_{NS}$, where M_{NS} is the mass of the neutron star [49]. Since neutrons inside compact objects can reach Fermi momenta of several hundred MeV, neutrons can decay to ADM for ADM particle masses less than $m_n + \mathcal{O}(k_{F,\chi}^2/2m_n)$, where m_n is the mass of the neutron. This process allows for total ADM masses of $\approx 0.05M_{NS}$ [49, 92]. Lastly, ADM can accumulate inside neutron stars via the production of ADM in supernovae. Since supernovae are very energetic events with luminosities in excess of $\mathcal{O}(10^{52} \text{ erg/s})$, they can efficiently produce ADM particles that can then be trapped within the newly born neutron star. As discussed in [92], supernovae events can produce total accumulated ADM masses up to about $0.15 M_\odot$ for MeV-scale ADM particles.

Although neutron Bremsstrahlung of ADM, neutron conversion of ADM, and production of ADM in supernovae each are capable of producing total ADM masses

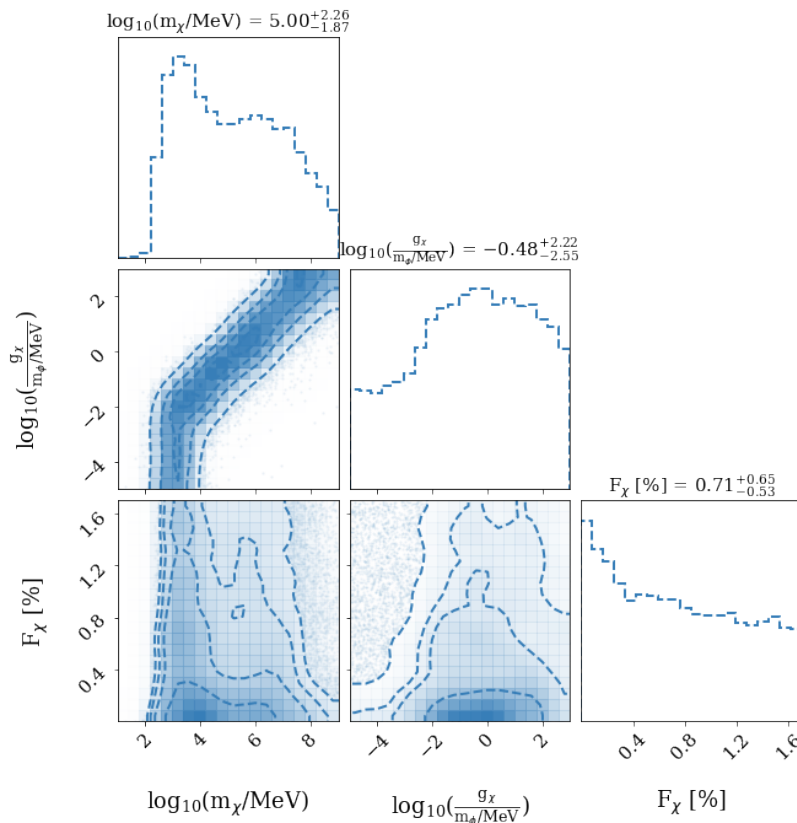


FIG. 1: Prior corner plot of the fermionic ADM EoS. Here, the ADM particle mass, effective self-interaction strength, and mass-fraction are plotted against each other, where the dark shaded regions represent a higher prior probability and lighter shaded regions represent a lower prior probability. The dashed blue lines in the 2-D contour plots represent the 0.5, 1, 1.5, and 2 σ contour levels. The top panels in each column show the 1-D prior histogram. The figure titles on the diagonal show the median value with the 0.16 and 0.84 fractional quantiles. In the $\log_{10}(m_\chi/\text{MeV})-\log_{10}(g_\chi/(m_\phi/\text{MeV}))$ plane we observe that the prior density has two large regions of no shading.

in the range of 0.02-0.15 M_\odot , all three of these processes are effective for ADM particle masses up to $\mathcal{O}(10^{2-3})$ MeV, which would only apply to a small fraction of the m_χ prior space. Since the aforementioned physically motivated mechanisms only apply to a few order magnitudes within the m_χ prior space, we choose not consider these ADM accumulation methods within our F_χ prior space. Other accumulation methods, such as a neutron star passing through an ADM over-density, accretion of baryonic matter onto a pre-existing ADM core, and a dark star-neutron star merger, could be considered [see 52, 92, and references therein]. However, such ADM accumulation mechanisms are highly speculative, thus we also neglect these accumulation methods. Therefore, to define the F_χ prior space, we will follow the upper bound ADM mass-fraction estimate of [50] using the Navarro-Frenk-White (NFW) dark matter mass density profile [102] to compute local dark matter density around our considered sources. The NFW dark matter profile is

given by

$$\rho_\chi(r) = \frac{\rho_0}{\frac{r_s}{r} \left(1 + \frac{r}{r_s}\right)^2}, \quad (21)$$

where $\rho_\chi(r)$ is the ADM mass density a radius, r , from the Galactic center (GC), $\rho_0 = 5.22 \pm 0.46 \cdot 10^7 M_\odot/\text{kpc}^3$ is the central density [103], $r_s = 8.1 \pm 0.7$ kpc is the scale radius [103]. By considering the F_χ approximation of [50], an upper limit on F_χ can be determined without a heavily restricted ADM particle mass prior space or having to consider a very hypothetical accumulation scenario.

In order to estimate the upper bound on F_χ , [50] calculated the ratio of the ADM mass density to the combined mass density of baryonic matter and ADM in the vicinity of PSR J0740+6620 and PSR J0348+0432, which are 8.6 kpc and 9.9 kpc from the GC, respectively. To model the baryonic mass density distribution, [50] used only the contribution of the Milky Way's stellar disc because both pulsars were taken to be sufficiently far away from the Galactic bulge. The shape of Galactic stellar disc

profile is

$$\rho_B(r) = \rho_{s,B} e^{-r/r_{s,B}}, \quad (22)$$

where $\rho_B(r)$ is baryonic mass density as a function of r , from the GC, $\rho_{s,B} = 15 M_\odot/\text{pc}^3$ is the baryonic mass density scale, and $r_{s,B} = 3.0$ kpc is the baryonic scale radius [104]. Since this work seeks to constrain fermionic ADM using neutron stars delivered by PPM, we will only consider PSR J0740+6620. Using the radial distance of PSR J0740+6620 to the GC, [50] found the F_χ upper bound near PSR J0740+6620 to be $F_\chi \leq 1.7\%$. By repeating the F_χ upper bound estimation for the two other PPM sources from *NICER*, we find that the maximum possible ADM mass-fraction is $\leq 1.54\%$ and $\leq 1.55\%$ for PSR J0030+0451 and PSR J0437–4715, respectively. Note, we have found the radial distances to the GC to be 8.32 kpc and 8.22 kpc, for PSR J0437–4715 and PSR J0030+0451, respectively. Therefore, because all three PPM delivered pulsars have similar F_χ upper estimates and PSR J0740+6620 can achieve the highest possible ADM mass-fraction, we adopt the upper bound on the ADM mass-fraction prior space to be

$$F_\chi \leq 1.7\%. \quad (23)$$

Lastly, we want to caution that the [50] calculation provides a best case upper estimate on F_χ in all of the *NICER* targets and that the true ADM mass-fraction in each pulsar due to their respective ADM surroundings is likely smaller than 1.7%.

Depending on the assumed ADM accumulation mechanism and scenario, the F_χ prior space can be constrained to be a finite size, but the effective fermionic ADM self-repulsion strength has yet to be physically constrained. In order to ensure that the g_χ/m_ϕ prior space is bounded from above, we adopt the upper bound of $g_\chi/m_\phi \leq 10^3 \text{ MeV}^{-1}$ to capture the highest self-repulsion strengths used in [38]. From below, g_χ/m_ϕ is physically allowed to be zero because the ADM fermionic degeneracy pressure provides enough support against gravitational collapse to a black hole. However, in Sec. II B, we have additionally assumed that $g_B \ll g_\chi$, thus a non-zero approximation to $g_\chi/m_\phi = 0 \text{ MeV}^{-1}$ is necessary. To accomplish this, we compute the relative radial percent difference (RRPD) between 0 MeV^{-1} and a small non-zero self-repulsion for various baryonic matter EoSs and pairs of (m_χ, F_χ) . We find that the RRPDs between $g_\chi/m_\phi = 10^{-5} \text{ MeV}^{-1}$ and zero self-repulsion do not exceed $4 \cdot 10^{-3}\%$. This shows that 10^{-5} MeV^{-1} is an adequate approximation for 0 MeV^{-1} down to mass-radius measurements with uncertainties $\mathcal{O}(10^{-3}\%)$ (see Appendix B for further details).

In summary, the fermionic ADM EoS prior space is taken to be

$$\log_{10}(m_\chi/\text{MeV}) \in [-2, 9] \quad (24)$$

$$F_\chi \in [0, 1.7]\% \quad (25)$$

$$\log_{10}\left(\frac{g_\chi}{m_\phi/\text{MeV}}\right) \in [-5, 3]. \quad (26)$$

Within each interval above, we uniformly sample each ADM parameter. We also assign all halo configurations to have a zero likelihood because the existence of any ADM halo has been shown to modify the pulse profile of neutron stars and thus the interpretation of the *NICER* mass-radius measurements [45]. This results in only ADM cores within the prior space. Moreover, within the remaining ADM core configurations, we also assign any ADM admixed neutron star with a mass $< 1M_\odot$ to have a zero likelihood evaluation. The minimum neutron star mass constraint is motivated by the theoretical description of a newly born neutron star [105]. In addition, the $1 M_\odot$ constraint is compatible with the minimum neutron star remnant masses from core-collapse supernovae simulations [see e.g., 106, 107]⁴. The consequences of the no-ADM halo and $1 M_\odot$ constraints can be seen as the non-shaded regions above and below the stripe in the $\log_{10}(g_\chi/(m_\phi/\text{MeV}))$ vs. $\log_{10}(m_\chi/\text{MeV})$ plot of Fig. 1. In Fig. 1, we show the prior corner plots of fermionic ADM EoS parameters, which shows a nonuniform distribution for all three fermionic ADM EoS parameters.

D. Source selection: real and synthetic

By considering both real and synthetic data, we will be able to demonstrate the current constraining power of *NICER*, and the potential future constraints of large area X-ray telescopes, like *STROBE-X*.

In order to assess the current capabilities of PPM delivered measurements, we consider the mass-radius posteriors of the *NICER* targets PSR J0740+6620 from [14] and PSR J0030+0451 from [18]. In top panel of Fig. 2, we show the mass-radius posteriors of PSR J0740+6620 of [14] and PSR J0030+0451 of [18] for our real data inferences.

Although the current mass-radius uncertainties on the *NICER* targets are at the $\sim 10\%$ level, it is interesting to consider the impact of future measurements in which more neutron stars will be observed at significantly lower mass-radius uncertainties. For the inferences where we consider synthetic neutron star mass-radius measurements, we model our sources using the *Future-X* scenario of [80]. The *Future-X* scenario assumes six sources in the mass range of $1.2 - 2.2 M_\odot$ with mass-radius uncertainties at the two percent level. This scenario is modeled after a best case possibility for the proposed NASA Probe mission *STROBE-X*, where *STROBE-X* performs long targeted observations of the six best candidates. We expect this scenario to deliver uncertainties at the two percent

⁴ We also want to note that our imposed $1 M_\odot$ constraint, although well supported, is in tension with the mass-radius measurement of the HESS J1731–347 supernova remnant [108]. However, this measurement is challenged by [109] because the [108] analysis relies on several assumptions about the distance to the star, the spectral modeling, and the data set chosen in analysis.

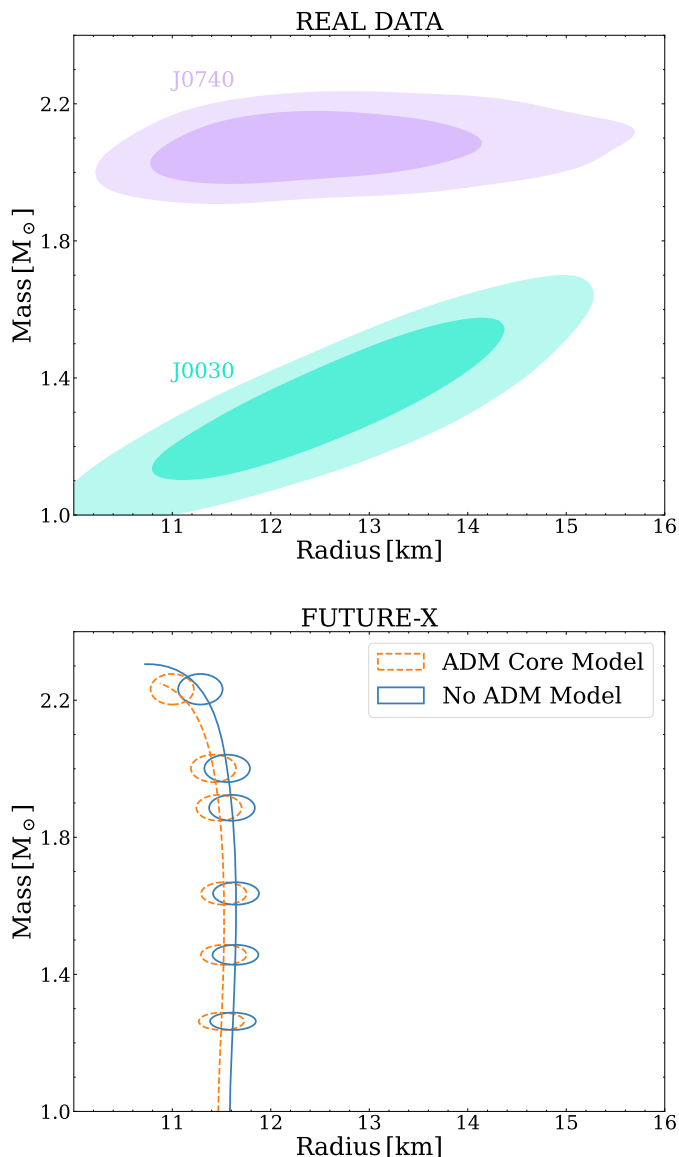


FIG. 2: Top panel: The 68% and 95% level uncertainty ellipses of the mass-radius measurements of PSR J0740+6620 from [14] and PSR J0030+0451 from [18]; Bottom panel: Uncertainty ellipses from the 1σ level of the 2-D Gaussian for each of the synthetic *Future-X* sources calculated from both ground truth models defined in Sec. IV B.

level, which would provide the strongest constraints on the neutron star EoS. The bottom panel of Fig. 2 shows the uncertainty ellipses corresponding to the *Future-X* scenario.

IV. RESULTS AND DISCUSSION

In all of our Bayesian parameter estimations, we take the most conservative approach of simultaneously varying all EoS parameters. By sampling all parameters in the neutron star EoS model, the most likely combined EoS of baryonic matter and fermionic ADM can be inferred. Additionally, this approach also allows for the constraints on the fermionic ADM EoS to be determined. In this section, we first study the posteriors of the fermionic ADM EoS and baryonic EoS using the mass-radius measurements of PSR J0740+6620 [14] and PSR J0030+0451 [18]. Using the synthetic data of the *Future-X* scenario, we again perform Bayesian inference on the fermionic ADM and baryonic matter EoSs to study the future promise of constraining fermionic ADM cores using neutron star mass-radius measurements.

A. Real data inferences

In Fig. 3, we show the posterior distributions on the fermionic ADM EoS in which we consider the mass-radius measurements of PSR J0740+6620 [14] and PSR J0030+0451 [18]. Here, the corner plot in the left panel of Fig. 3 shows that all of the 1-D histograms and 2-D posterior density contours strongly overlap with their respective priors. From the observation that the fermionic ADM priors and posteriors are approximately identical, we conclude that the fermionic ADM EoS parameters cannot be constrained under the chosen priors and current uncertainties of the baryonic EoS. However, if the fermionic ADM posteriors and priors are transformed into the $\log_{10} \left(\frac{g_\chi}{(m_\phi/\text{MeV})} / (m_\chi/\text{MeV}) \right) - F_\chi$ plane (right panel of Fig. 3), we find that the lower bound on the ratio of g_χ/m_ϕ and m_χ can be constrained when compared to the prior. In particular, we find that the prior 68% (95%) credible levels on $\log_{10} \left(\frac{g_\chi}{(m_\phi/\text{MeV})} / (m_\chi/\text{MeV}) \right)$ is $-5.7^{+1.08}_{-1.16}$ ($5.7^{+1.49}_{-1.91}$). For the posteriors, we find the 68% (95%) credible levels to be $-5.62^{+0.97}_{-0.97}$ ($5.62^{+1.36}_{-1.75}$). Thus, the lower bound on $\log_{10} \left(\frac{g_\chi}{(m_\phi/\text{MeV})} / (m_\chi/\text{MeV}) \right)$ can be constrained to -6.59 and -7.36 at the 68% and 95% credible levels, respectively. The lower bound on the ratio of g_χ/m_ϕ and m_χ can be constrained while the upper bound cannot because small ratios produce compact ADM cores with ADM central densities that are several orders of magnitude larger than the baryonic central densities for a given F_χ , which significantly reduce the resulting neutron star mass below the $1M_\odot$ constraint. While, for the same F_χ , large ratios of g_χ/m_ϕ and m_χ produce more diffuse fermionic ADM cores with ADM central densities less than baryonic central energy densities, which affect the overall neutron star mass less than the lower ratios. For instance, for $\log_{10} \left(\frac{g_\chi}{(m_\phi/\text{MeV})} / (m_\chi/\text{MeV}) \right) = -8$ and $F_\chi = 0.75\%$, the maximum central ADM den-

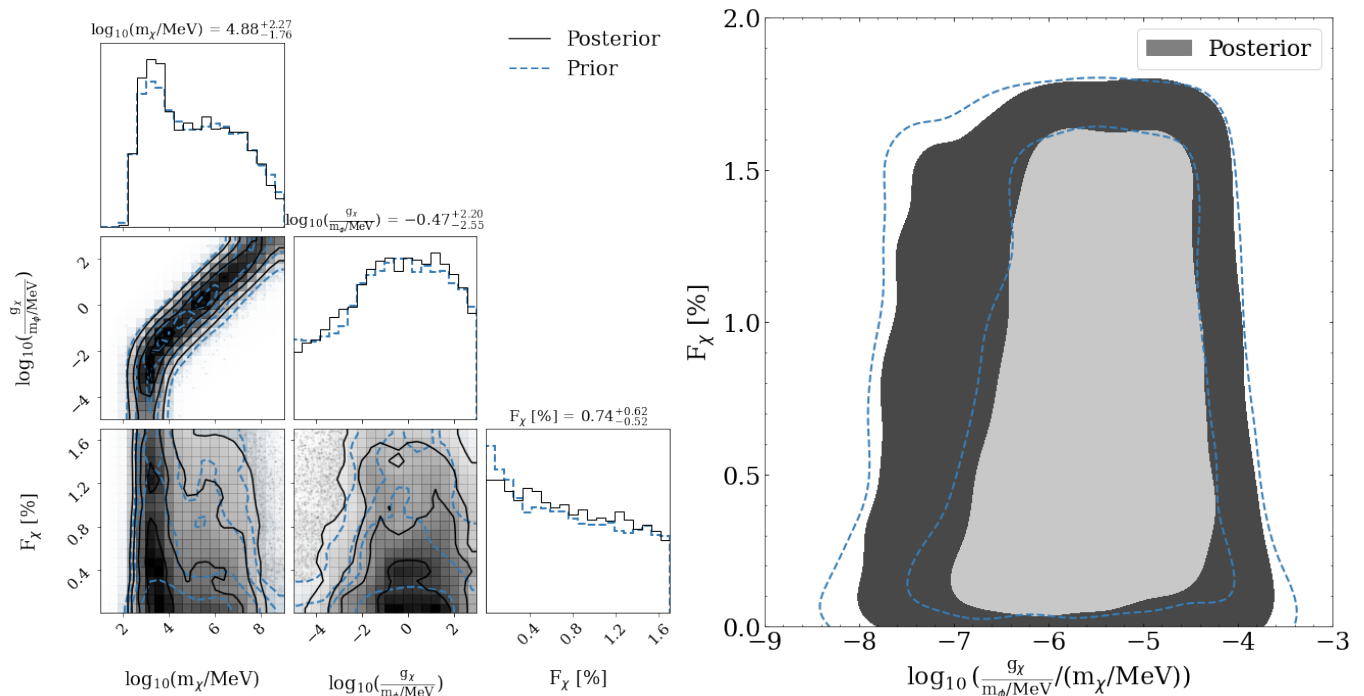


FIG. 3: Left panel: Posterior distribution of the fermionic ADM EoS parameters (solid black lines) in which real data is considered. For comparison, we have overlaid the posteriors with their respective priors (dashed blue lines). The contour levels are same as in Fig. 1; Right panel: Probability density contour plot of the ADM posteriors in the F_χ vs. $\log_{10}\left(\frac{g_x}{(m_\phi/\text{MeV})/(m_\chi/\text{MeV})}\right)$ plane. Note, the contours represent the 1 σ (light grey) and 2 σ (dark grey) levels for both the prior and posterior. Here we see that the 1 σ level posteriors favor slightly higher ratios of g_x/m_χ and m_χ , but the 2 σ posteriors are almost touching the priors for all F_χ . In the left panel, we find that the priors and posteriors are nearly identical in all panels. However, in the right panel, we find that the 1 σ and 2 σ level posteriors favor slightly higher ratios of g_x/m_χ and m_χ than their respective priors.

sity is $\approx 10^{20} g/cm^3$ and the maximum central baryonic density is $\approx 10^{15} g/cm^3$, which results in the maximum neutron star mass of $\approx 0.86 M_\odot$. However, if we again take $F_\chi = 0.75\%$ and the same maximum baryonic central density, but $\log_{10}\left(\frac{g_x}{(m_\phi/\text{MeV})/(m_\chi/\text{MeV})}\right) = -4$, the maximum central ADM density is reduced to $\approx 10^{13.4} g/cm^3$ and the maximum neutron star mass increases to $2.38 M_\odot$.

In Fig. 4, the priors and posteriors of Fig. 3 are converted to the pressure-energy density plane (left) to study the effect that fermionic ADM cores have on the uncertainties of the baryonic EoS⁵. In particular, we consider the EoS posteriors that only vary the baryonic EoS (‘Neglecting ADM’) and the EoS posteriors that additionally vary the ADM EoS (‘Including ADM’). Fig. 4 shows that the 95% confidence region of the ‘Including ADM’ band (orange dashed dotted band) is marginally wider than the 95% confidence region of the ‘Neglecting ADM’ band

(light green band). Quantitatively, we calculate that the ‘Including ADM’ band is 1.39% and 0.71% wider than the ‘Neglecting ADM’ band at $\log_{10}(\epsilon cm^3/g) = 14.38$ and $\log_{10}(\epsilon cm^3/g) = 15.008$, respectively. Accounting for the possibility of fermionic ADM cores broadens the uncertainties on the baryonic EoS because ADM cores decrease the neutron star mass and radius, which allows the baryonic EoS to be more stiff and remain in agreement with the source data. However, since including fermionic ADM broadens the 95% confidence interval on the baryonic EoS by $\mathcal{O}(1\%)$, we conclude that fermionic ADM cores do not significantly impact the uncertainties on the baryonic EoS within the considered ADM priors.

Fig. 4 additionally shows the posterior distributions on the both the fermionic ADM admixed neutron star mass-radius relation (‘Including ADM’) and the purely baryonic mass-radius relation (‘Neglecting ADM’). Along the radial axis, Fig. 4 shows that the ‘Including ADM’ contours predict similar radii to the ‘Neglecting ADM’ contours. Fig. 4 also shows that the ‘Including ADM’ band favor marginally lower maximum masses than the ‘Neglecting ADM’ band. In particular, the 68% and 95% confidence regions of the ‘Including ADM’ predict

⁵ Note, we have scaled the energy density by a factor of c^{-2} such that it has units of g/cm^3 .

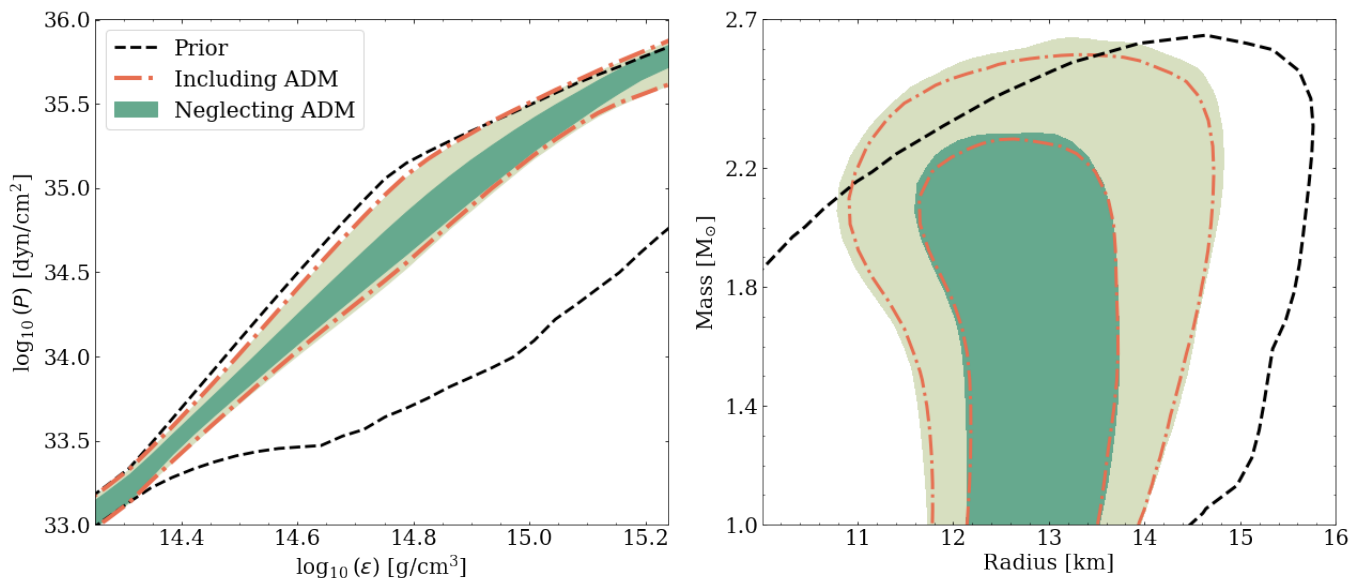


FIG. 4: Left panel: Pressure-energy density posterior and prior distributions for the baryonic EoS for when fermionic ADM is included and neglected; Right panel: Mass-radius posterior and prior distributions for the total combined ADM and baryonic equations of state for when fermionic ADM is included and neglected. For both panels, the black dashed line represents the 95% prior distribution, the orange dashed-dotted lines represent the 68% and 95% confidence regions of the posteriors that vary both the baryonic and fermionic ADM EoS parameters, and the light/dark green regions are the 68% and 95% confidence regions of the posteriors that only vary the baryonic EoS. Note, in the left panel we only show the 95% confidence region of the ‘Including ADM’ band. Here we see that the ‘Including ADM’ bands are nearly identical to the ‘Neglecting ADM’ bands in both panels.

maximum masses of $2.287 M_{\odot}$ and $2.525 M_{\odot}$, respectively. While the ‘Neglecting ADM’ band predicts maximum masses of $2.308 M_{\odot}$ and $2.573 M_{\odot}$ for the 68% and 95% confidence regions, respectively. The ‘Including ADM’ posterior favors lower maximum masses than the ‘Neglecting ADM’ posterior because ADM cores decrease neutron star masses when compared to an identical neutron star with the same baryonic central energy density. This reduction in mass from the presence of ADM cores would push the posteriors to predict lower maximum masses than inferences done with only baryonic matter. Since the ‘Including ADM’ band only marginally favors lower maximum masses, we find that the inclusion of fermionic ADM cores is fully consistent with the mass-radius posteriors in which only baryonic matter is accounted for. This highlights that, under the current uncertainties of PPM delivered neutron star mass-radius measurements, the presence of fermionic ADM cores in neutron star interiors cannot be ruled out.

B. Synthetic data inferences

We now consider the synthetic mass-radius measurements of a potential *STROBE-X* scenario using the *Future-X* scenario of [80]. To study such a potential scenario, it is useful to define two ground truth models i.e., models in which the synthetic neutron star mass-radius

measurements will be computed from: one with an ADM core and one with only baryonic matter. Considering two ground truth models will allow for statements about the ADM EoS, regardless if ADM cores are actually present in neutron stars. The first ground truth model that we consider is the ‘ADM Core’ model, which is described by the PP model in Sec. II B with an ADM core defined by the ADM parameters

$$m_{\chi} = 15 \text{ GeV} \quad (27)$$

$$\frac{g_{\chi}}{m_{\phi}/\text{MeV}} = 0.01 \quad (28)$$

$$F_{\chi} = 1.5\%. \quad (29)$$

The second ground truth model is defined identically to the ‘ADM core’ model, but $F_{\chi} = 0\%$ in order to account for the possibility that neutron stars do not accumulate an appreciable total ADM mass, but the possibility of ADM is still considered during sampling. Using the *Future-X* scenario with the ‘No ADM’ and ‘ADM core’ models in this way will allow for the best-case future constraints on fermionic ADM to be determined [see 80]. In Fig. 2, the uncertainty ellipses and ground truth models for the *Future-X* scenario are shown.

In Fig. 5, we show the fermionic ADM prior and posterior distributions of the ‘No ADM’ (left) and ‘ADM Core’ (right) models for the *Future-X* scenario. In the top two panels, we show the corner plots of the ‘No ADM’ and ‘ADM Core’ models. In both the 2-D density

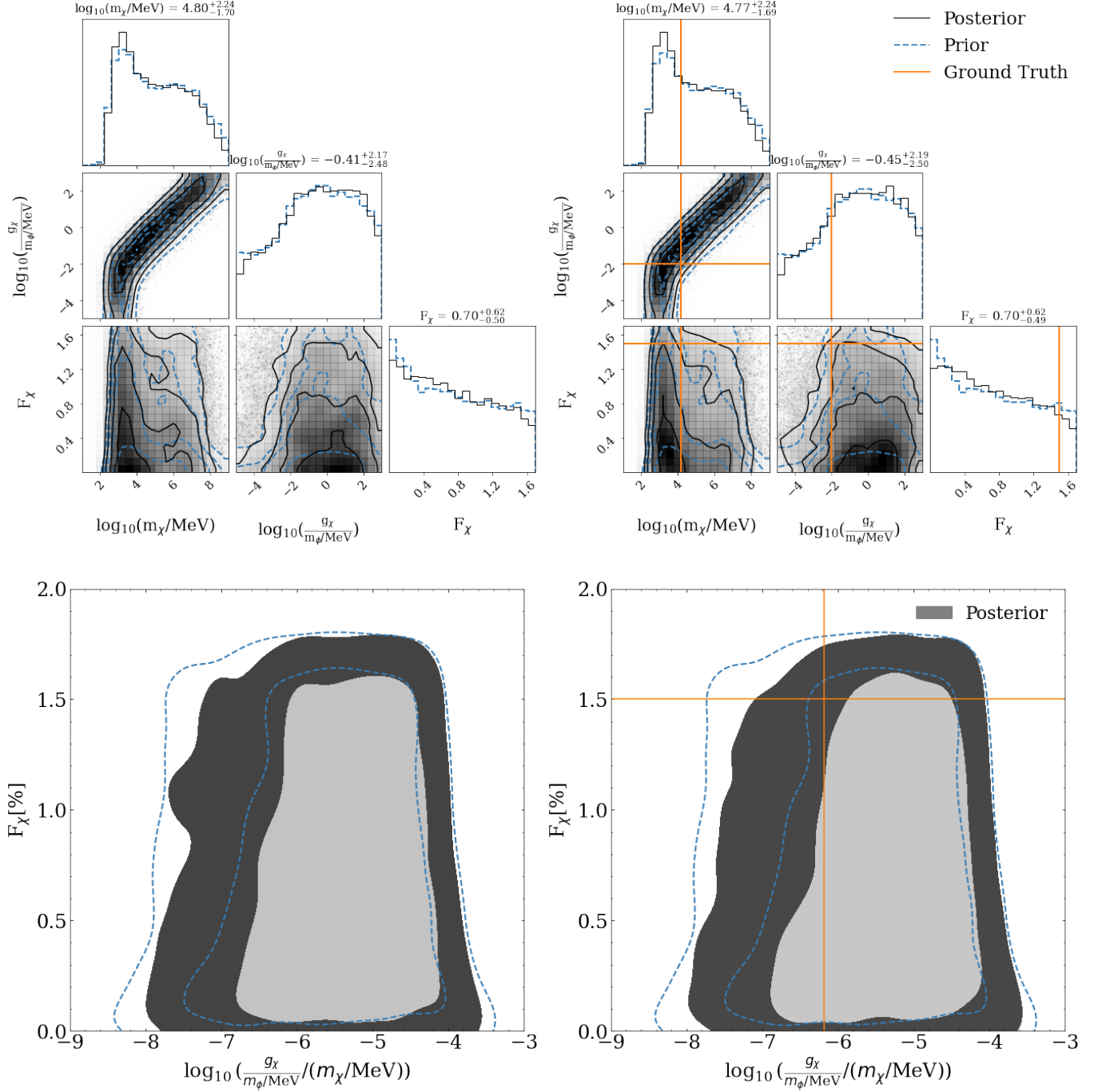


FIG. 5: Left two panels: *Future-X* fermionic ADM posteriors for the “No ADM” model; Right two panels: Same as the left two panels, but for the “ADM Core” model. The top two panels are the corner plots of the fermionic ADM EoS posteriors for the “No ADM” and “ADM Core” ground truth models. The posterior and prior contour levels of the upper panels are same as in Fig. 3. In the bottom panels, we show the fermionic ADM posteriors and priors in the $\log_{10}(\frac{g_x}{m_\phi/\text{MeV}}/(m_\chi/\text{MeV}))$ - F_χ plane. The contour levels of both the priors and posteriors are identical to the levels of Fig. 3. In all panels, the orange solid lines represent the ground truth values for the “ADM Core” model. We find that the corner plots of both ground truth models are approximately identical to one another, while the bottom contour plots differ slightly along the F_χ -axis.

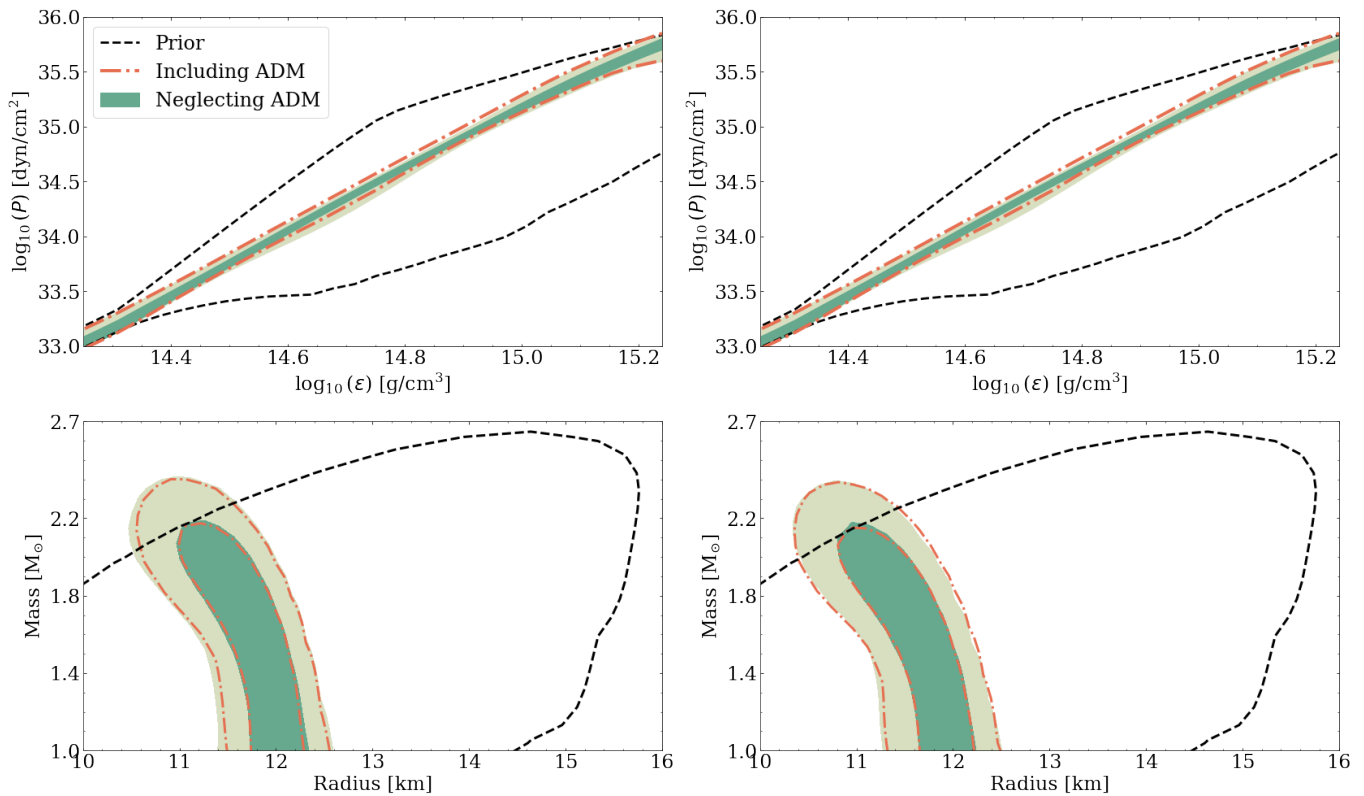


FIG. 6: Left two panels: *Future-X* fermionic ADM and baryonic matter EoS posteriors and priors of the “No ADM” model converted to the pressure-energy density plane (top panel) and mass-radius plane; Right two panels: Same as the left two panels, but for the “ADM Core” model. Note, the top two panels following the same legend and contour levels as Fig. 4, and the bottom two follow the same legend and contour levels as Fig. 5. Note, the solid orange lines in the bottom two panels are the “No ADM” and “ADM Core” model ground truth mass-radius curves, respectively. In all quadrants, we find that the ‘Including ADM’ bands are nearly identical to the ‘Neglecting ADM’ bands.

and 1-D histograms plots, the posteriors of both ground truth models are identical to each other, despite having different ground truth ADM mass-fractions. In addition, the posterior distributions of the “ADM Core” and “No ADM” models are approximately identical to the prior distribution. Since the corner plots of both the “No ADM” and “ADM Core” models are nearly identical to each other as well as the prior, the *Future-X* scenario will not be able to provide any additional constraints on the fermionic ADM particle mass, effective self-repulsion strength, and mass-fraction than the inferences using the neutron star data from [14, 18].

In the bottom two panels of Fig. 5, the fermionic ADM posteriors and priors are transformed to the $\log_{10}\left(\frac{g_\chi}{m_\phi/\text{MeV}}/(m_\chi/\text{MeV})\right)-F_\chi$ plane. Fig. 5 shows that the “ADM Core” model posteriors narrow on the left side more than the “No ADM” posteriors for increasing F_χ . The posteriors on the ratio of g_χ/m_ϕ and m_χ differ along the F_χ axis because the ground truth mass-fractions are 1.5% and 0% for the “ADM Core” and “No ADM” models, respectively. That is, a given ratio of g_χ/m_ϕ and m_χ could produce mass-radius curves satisfying the “No

ADM” model data for F_χ near 0%, but simultaneously not produce neutron stars satisfying the “ADM Core” model data for $F_\chi \approx 1.5\%$. Since the posteriors on the ratio of the fermionic ADM self-repulsion and particle mass differ between both ground truth models and the priors, we find that *Future-X* will be able to constrain the lower bound on the ratio of g_χ/m_ϕ and m_χ . In particular, the lower bound on $\log_{10}\left(\frac{g_\chi}{m_\phi/\text{MeV}}/(m_\chi/\text{MeV})\right)$ is constrained to be $\gtrsim -6.5$ and $\gtrsim -7.29$, at the 68% and 95% confidence intervals, respectively. However, when compared to the real data posteriors of Fig. 3, the *Future-X* scenario can only slightly tighten the constraints on $\log_{10}\left(\frac{g_\chi}{m_\phi/\text{MeV}}/(m_\chi/\text{MeV})\right)$ at both the 68% and 95% confidence intervals.

Fig. 6 shows the “No ADM” and “ADM Core” model posteriors on the baryonic EoS uncertainty in the pressure-energy density plane (top two panels) and the combined fermionic ADM and baryonic matter EoS in the mass-radius plane (bottom two panels). In the pressure-energy density plane, the 95% confidence region of the ‘Including ADM’ predicts baryonic EoS uncer-

tainties that are comparable to those of the ‘Neglecting ADM’ band for both the “No ADM” and “ADM Core” models. In the mass-radius plane, the 68% and 95% confidence intervals on the ‘Including ADM’ band also do not significantly deviate from their corresponding ‘Neglecting ADM’ bands. Based on the observations that the ‘Including ADM’ bands favor nearly identical posteriors to the ‘Neglecting ADM’ bands, this figure shows that fermionic ADM cores do not affect the posteriors on the neutron star mass-radius relation and the uncertainties on the baryonic EoS. Thus, we conclude that the presence of fermionic ADM cores in neutron star interiors can remain consistent with baryonic matter inferences down to the 2% mass-radius uncertainty level.

V. SUMMARY AND CONCLUSIONS

In this work, we have presented a full Bayesian analysis for fermionic ADM cores in neutron stars using the framework developed in [80]. Here we have modeled the fermionic ADM cores using the [38] ADM model, which describes ADM as spin-1/2 fermions with repulsive self-interactions. We have considered the mass-radius data of PSR J0740+6620 [14] and PSR J0030+0451 [18] as well as synthetic mass-radius data from a best case scenario of the NASA *STROBE-X* mission. By considering both real and synthetic mass-radius measurements, we inferred the current and possible future constraints on the fermionic ADM particle mass m_χ , effective self-repulsion strength g_χ/m_ϕ , and mass-fraction F_χ .

For the inferences which consider the PSR J0740+6620 and PSR J0030+0451 mass-radius measurements, we find that the 2-D posterior densities of $\log_{10}(m_\chi/\text{MeV})$ vs. $\log_{10}(g_\chi/(m_\phi/\text{MeV}))$, F_χ vs. $\log_{10}(m_\chi/\text{MeV})$, and F_χ vs. $\log_{10}(g_\chi/(m_\phi/\text{MeV}))$ are nearly identical to their respective prior densities. In addition, the 1-D posterior histograms of each fermionic ADM EoS parameter also strongly coincide with their prior counterparts. However, if the ADM posteriors are transformed to the $\log_{10}\left(\frac{g_\chi}{m_\phi/\text{MeV}}/(m_\chi/\text{MeV})\right)$ - F_χ plane, the lower bound on the ratio of the fermionic ADM effective self-repulsion strength to the particle mass can be constrained to -6.59 and -7.36 at the 68% and 95% confidence levels, respectively. These results show that, within the current uncertainties of neutron star mass-radius measurements delivered by *NICER*, the lower bound of the ratio of g_χ/m_ϕ and m_χ can only be marginally constrained. On the other hand, all other combinations of fermionic ADM parameters cannot be constrained.

Converting the fermionic ADM and baryonic matter EoS posteriors to the mass-radius and pressure-energy density planes, we find that the posteriors on the neutron star EoS are largely unaffected by the inclusion of fermionic ADM cores. In the mass-radius plane, we find that the maximum masses of the posteriors which include

fermionic ADM differ from the purely baryonic ones at the 95% percent level by $0.048 M_\odot$. Moreover, the combined fermionic ADM and baryonic mass-radius posteriors predict similar radii to the purely baryonic posteriors. In the pressure-energy density plane, the baryonic EoS uncertainty slightly broadens when fermionic ADM is accounted for. In particular, at $\log_{10}(\varepsilon \text{ cm}^3/\text{g}) = 14.38$ and , the baryonic EoS uncertain widens by 1.39%. The small differences between the posteriors that include fermionic ADM cores and the ones that do not, show that fermionic ADM cores inside neutron star interiors can be fully consistent with their purely baryonic counterparts.

In order to determine the promise of constraining fermionic ADM cores by missions, like the NASA *STROBE-X* mission, this work has also considered the *Future-X* scenario from [80]. The *Future-X* scenario describes six synthetic neutron star mass-radius measurements with mass and radius uncertainties at the 2% level. Within the *Future-X* scenario, the fermionic ADM posteriors remain nearly identical to the real data inferences for both the “ADM core” and “No ADM” models. However, we find that the posteriors on the ratio of g_χ/m_ϕ and m_χ differ between the “No ADM” and “ADM core” models. In particular, the “ADM core” mode infers marginally tighter constraints on the lower bound of $\log_{10}\left(\frac{g_\chi}{m_\phi/\text{MeV}}/(m_\chi/\text{MeV})\right)$ than the “No ADM” model. The posteriors on the lower bound of $\log_{10}\left(\frac{g_\chi}{m_\phi/\text{MeV}}/(m_\chi/\text{MeV})\right)$ are slightly more narrow in the “ADM core” model than in the “No ADM” model because the ground truth mass-fraction of the “ADM core” model is higher than that of the “No ADM” model. This allows for ratios of g_χ/m_ϕ and m_χ , which produce neutron stars satisfying the “No ADM” data for a given F_χ , to be given a non-zero likelihood. However, the same ratios of g_χ/m_ϕ and m_χ would be given a zero likelihood because they would not satisfy the data of the “ADM core” model for the same given F_χ . Since the posteriors in $\log_{10}\left(\frac{g_\chi}{m_\phi/\text{MeV}}/(m_\chi/\text{MeV})\right)$ - F_χ plane differ between the “No ADM” and “ADM core” models, we found that *Future-X* will be able to constrain the lower bound the ratio of g_χ/m_ϕ and m_χ .

According to the posteriors on the lower bound of ratio of g_χ/m_ϕ and m_χ , we find that *Future-X* slightly tightens the constraints to -6.5 and -7.29 at the 68% and 95% confidence levels, respectively. It is physically reasonable that the constraints on $\log_{10}\left(\frac{g_\chi}{m_\phi/\text{MeV}}/(m_\chi/\text{MeV})\right)$ improve in the *Future-X* scenario because the mass of an admixed neutron star is sensitive to the compactness of the fermionic ADM core, which is partially controlled by the ratio of g_χ/m_ϕ and m_χ . Therefore, the posteriors on the lower bound of $\log_{10}\left(\frac{g_\chi}{m_\phi/\text{MeV}}/(m_\chi/\text{MeV})\right)$ will slightly improve with the tighter mass and radius uncertainties of the *Future-X* scenario. Note, however, the *Future-X* scenario is a best case scenario for the *STROBE-X* mission and our constraints will relax accordingly for larger

mass-radius credible intervals.

In the pressure-energy density and mass-radius plane, we find that the uncertainties on the baryonic matter EoS and the total neutron star mass-radius remain unaffected when the possibility of fermionic ADM cores is considered. That is, similar to the real data inferences, we find that the pressure-energy density and mass-radius of the ‘Including ADM’ bands are identical to their respective ‘Neglecting ADM’ bands in both the “No ADM” and “ADM core” models. Our results highlight that neutron star EoS models that additionally allow for fermionic ADM cores are consistent with baryonic EoS inferences for mass and radius uncertainties down to the 2% level. Finally, under the current and potential future uncertainties of the baryonic EoS, the possible presence of fermionic ADM cores can be undetected by both *NICER* and *STROBE-X*.

The ‘Including ADM’ posteriors of both the real data from *NICER* and the hypothetical data from the *Future-X* scenario (*STROBE-X*) are physically consistent with the ‘Neglecting ADM’ posteriors in part because, under the ADM mass-fraction priors considered, the separations between the fermionic ADM admixed mass-radius curves and their purely baryonic counterparts are smaller than the size of the uncertainty ellipses of the data. This is most clearly shown in Fig. 2, where the “ADM core” and “NO ADM” uncertainty ellipses strongly overlap for all sources. The other reason why including fermionic ADM cores is physically consistent with the baryonic matter posteriors is because of the strong degeneracy between the a softer baryonic EoS and another stiffer baryonic EoS with a fermionic ADM core. Our results show this in the mass-radius posteriors of Figs. 4 and 6, where the purely baryonic posteriors strongly overlap with the fermionic ADM posteriors. Lastly, [61] pointed out several scenarios that could break this degeneracy, such as a reduction of neutron star masses toward the center of the Galaxy, searching for supplementary peaks in gravitational wave spectra from binary neutron star merger simulations, detecting objects that are in contrast to our understanding of neutron star structure, and by finding a new feature in the binary Love relation.

Overall, this work shows that the current neutron star measurement of the NASA *NICER* mission, as well as the potential future measurements of the NASA *STROBE-X* mission, will be able to provide constraints on the lower bound of the ratio g_χ/m_ϕ and m_χ , but not the individual quantities of F_χ , m_χ , and g_χ/m_ϕ . Moreover, within the uncertainties on the baryonic EoS, we find that the presence of fermionic ADM cores can remain consistent with inferences that only include baryonic matter. This implies that neither *NICER* nor *STROBE-X* will be able to discern its presence. Although fermionic ADM cores could go undetected by *NICER* and *STROBE-X*, when specific assumptions about the neutron EoS are made, small ADM mass-fractions have been shown to trigger rapid neutron star cooling for low mass neutron stars through the direct Urca process, which could shed light

on the presence of ADM in these stars [55, 110, 111].

Future work will explore how the proper inclusion of fermionic (as well as bosonic) ADM halos affects our inferences on both the ADM and baryonic matter EoSs. The work of [45] constructed a framework for interpreting neutron star mass-radius measurements in the presence of ADM halos. While many works consider a variety of different plausible ADM mass-fractions [see e.g., 45–47, 49, 52, 56, 59, 92, 112, and references therein], an in-depth analysis on the possible accumulation methods of ADM in neutron stars has yet to be done and is left for future work. By appropriately accounting for the possible presence of ADM halos and physically constraining F_χ , full inferences on the neutron star EoS will be able to determine the most general constraints on the ADM EoS.

ACKNOWLEDGMENTS

We acknowledge Ann Nelson for her pioneering work on dark matter in neutron stars. We thank Michael Lathwood for insightful conversations with N.R. on the consequences of the symmetric nature of the metric tensor. We also thank Nathan Musoke, Yves Kini, Anthony Mirasola, and Melissa Mendes for feedback on the manuscript. A.L.W. acknowledges support from ERC Consolidator grant No.865768 AEONS. C.P.W. acknowledges all the administrative and facilities staff at the University of New Hampshire, especially Katie Makem-Boucher and Michelle Mancini. The contributions of C.P.W. and N.R. were supported by NASA grant No.80NSSC22K0092.

Software: Python/C language [113], GNU Scientific Library [GSL; 114], NumPy [115], Cython [116], SciPy [117], MPI for Python [118], Matplotlib [119], Jupyter [120], MultiNest [121], PYMULTINEST [122], kalepy [123], corner [124], seaborn [125], NEST [99].

Appendix A: From Lagrangian to EoS: the fermionic ADM model

The Lagrangian of the [38] fermionic ADM model discussed in Sec. II is given by, in units of $\hbar = c = 1$,

$$\mathcal{L}_\chi = -\sqrt{-g}[\bar{\chi}(i\gamma_\mu D^\mu + m_\chi)\chi + \frac{1}{2}m_\phi^2\phi_\mu\phi^\mu + \frac{1}{4}Z_{\mu\nu}Z^{\mu\nu} - g_B\phi_\mu J_B^\mu]. \quad (\text{A1})$$

As discussed in Sec. IIB, we make two approximations in order to simplify the Eq. A1. First, we assume $g_B \ll g_\chi$, which allows for the interaction term between ADM and baryonic matter in Eq. A1 to be neglected, i.e., $g_B\phi_\mu J_B^\mu$. Second, following [52], we assume that the derivatives of the metric are small compared to the inverse length scales of neutron stars, thus the spacetime can be taken to be flat. This can be shown explicitly by considering a

typical neutron star of $R = 10$ km and a spherical layer of thickness $\delta r = 10^{-3}$ km, which is chosen to be large enough to treat ADM thermodynamically. At the stellar surface, the gradient of the g_{tt} component of the metric can be shown to be

$$\left| \frac{dg_{tt}}{dr} \right| \delta r < \frac{\delta r}{R} = 10^{-4}. \quad (\text{A2})$$

Therefore the fluctuations of the metric at the neutron star surface compared to the flat metric are small and we can approximate the spacetime to be flat. For further details, we refer the reader to Appendix A of [80] or [52].

Under the flat spacetime approximation and the assumption that $g_B \ll g_\chi$, the Lagrangian can be simplified to

$$\mathcal{L}_\chi = -\sqrt{-g} [\bar{\chi} (i\gamma_\mu D^\mu + m_\chi) \chi + \frac{1}{2} m_\phi^2 \phi_\mu \phi^\mu + \frac{1}{4} Z_{\mu\nu} Z^{\mu\nu}]. \quad (\text{A3})$$

Upon varying the action with respect to χ , $\bar{\chi}$, and ϕ_μ , the equations of motion Eqs. 9, 10, and 11 are obtained. Within the mean-field approximation, the ϕ_μ field operator, which we treat as a classical field, is replaced by its ground state ($|\Phi\rangle$) expectation value, thus $\langle \Phi | \phi_\mu | \Phi \rangle = \langle \phi_\mu \rangle = (\phi_0, \mathbf{0})$. Inserting the expression for $\langle \phi_\mu \rangle$ into the equation of motion for ϕ_μ , we find

$$\phi_0 = \frac{g_\chi}{m_\phi^2} \langle \chi^\dagger \chi \rangle = \frac{g_\chi}{m_\phi^2} n_\chi, \quad (\text{A4})$$

where n_χ is the ADM number density. Note, we have used the fact that n_χ is given by the first element of the conserved current of the ADM Lagrangian, J^μ , via $J_0 = -J^0 = \langle \chi^\dagger \chi \rangle$, where $\langle \chi^\dagger \chi \rangle$ is the normal-ordered expectation value of $\chi^\dagger \chi$ with respect to the ground state.

Next, since we have employed the mean-field approximation, we replace the ADM field operators by their normal-ordered ground state expectation values [see 126, 127, which applied the mean-field approximation to spin-1/2 Dirac fermion fields in the context of the σ - ω model]. The relevant ADM field operator expectation values can be obtained by computing the stress-energy tensor, which is calculated by varying the action with respect to the metric [128]. Within the mean-field approximation, we find the stress-energy tensor to be

$$T_{\mu\nu} = i\bar{\chi}\gamma_\mu\nabla_\nu\chi - \frac{g_{\mu\nu}}{2}m_\phi^2\phi_\mu\phi^\mu. \quad (\text{A5})$$

The relevant ADM field operators are given in the first terms of T_{00} and $(T_{11} + T_{22} + T_{33})/3$, which correspond to the ADM energy density (ϵ_χ) and pressure (p_χ), respectively. As a result, the ground state expectation values of the ADM field operators that need to be calculated are

$$\langle \Phi | : \chi^\dagger \chi : | \Phi \rangle = \langle \chi^\dagger \chi \rangle \quad (\text{A6})$$

$$\langle \Phi | : i\chi^\dagger \nabla_0 \chi : | \Phi \rangle = \langle i\bar{\chi}\gamma_0\nabla_0\chi \rangle \quad (\text{A7})$$

$$\frac{1}{3} \langle \Phi | : i\bar{\chi}(\gamma \cdot \nabla)\chi : | \Phi \rangle = \frac{1}{3} \langle i\bar{\chi}(\gamma \cdot \nabla)\chi \rangle, \quad (\text{A8})$$

where $::$ is the normal ordering operator. According to [126], we can compute the expectation values of Eqs. A6 and A7 via

$$\langle \bar{\chi}\Gamma\chi \rangle = \sum_s \int \frac{d^3k}{(2\pi)^3} (\bar{\chi}\Gamma\chi)_{k,s} \Theta[E_{\text{Fermi}} - e(\mathbf{k})], \quad (\text{A9})$$

where Γ is a general field operator, \sum_s is the sum over single-particle spin states (s), $(\bar{\chi}\Gamma\chi)_{k,s}$ is the expectation value of the single-particle state with momentum k and spin s , E_{Fermi} is the Fermi energy of a single particle in the mean-field approximation, $e(\mathbf{k})$ is ADM energy eigenvalues for a single particle with momentum \mathbf{k} , and $\Theta[E_{\text{Fermi}} - e(\mathbf{k})]$ is the Heaviside step function, which is taken to be one for $x \geq 0$ and zero otherwise.

In order to obtain the ADM energy eigenvalues, $e(\mathbf{k})$, we first apply the mean-field approximation to the equation of motion for the ADM field, χ , which results yields

$$[i\gamma^\mu(\nabla_\mu + ig_\chi\phi_\mu) + m_\chi]\chi(x) = 0. \quad (\text{A10})$$

Since all of the terms Eq. A10 are independent of x under the mean-field approximation, $\chi(x)$, and by extension $\bar{\chi}(x)$, are momentum eigenstates of the form

$$\chi(x) = \chi(k)e^{-ik \cdot x} \quad (\text{A11})$$

$$\bar{\chi}(x) = \bar{\chi}(k)e^{+ik \cdot x}, \quad (\text{A12})$$

where $k \cdot x = k_\mu x^\mu$ and $k_\mu = (e(\mathbf{k}), \mathbf{k})$ [126]. By inserting Eq. A11 into Eq. A10, defining $K_\mu = k_\mu - g_\chi\phi_\mu$, and scaling the result by $\gamma^\nu K_\nu - m_\chi$, we find that

$$K_\mu K^\mu + m_\chi^2 = 0 \quad (\text{A13})$$

$$\implies K_0 = \sqrt{K_i K^i + m_\chi^2} \quad (\text{A14})$$

$$\implies e(\mathbf{k}) = k_0 = \sqrt{k^2 + m_\chi^2} + g_\chi\phi_0. \quad (\text{A15})$$

Additionally, by inserting Eqs. A11 and A12 into Eq. A6, A7, and A8, the ground state expectation values become

$$\langle \chi^\dagger \chi \rangle \quad (\text{A16})$$

$$\langle \chi^\dagger k_0 \chi \rangle \quad (\text{A17})$$

$$\frac{1}{3} \langle \bar{\chi} \gamma \cdot \mathbf{k} \chi \rangle. \quad (\text{A18})$$

In order to evaluate the single-particle expectation value in Eqs. A17, we again follow [126] and solve for the ADM Hamiltonian by isolating k_0 in Eq. A10, which yields

$$H_{ADM} = \gamma_0 [\gamma \cdot \mathbf{k} + g_\chi\gamma_0\phi_0 + m_\chi]. \quad (\text{A19})$$

We then note that $\partial H_{ADM}/\partial k = \gamma_0\gamma$. Therefore, the expectation values of Eqs. A16, A17, and A8 can be ex-

pressed in terms of $e(\mathbf{k})$.

$$\langle \chi^\dagger \chi \rangle = \sum_s \int \frac{d^3k}{(2\pi^2)^3} (\chi^\dagger \chi)_{k,s} \Theta \quad (\text{A20})$$

$$\langle \chi^\dagger k_0 \chi \rangle = \sum_s \int \frac{d^3k}{(2\pi^2)^3} (\chi^\dagger e(\mathbf{k}) \chi)_{k,s} \Theta \quad (\text{A21})$$

$$\frac{1}{3} \langle \bar{\chi} \boldsymbol{\gamma} \cdot \mathbf{k} \chi \rangle = \sum_s \int \frac{d^3k}{3(2\pi^2)^3} \left(\chi^\dagger \frac{\partial e(\mathbf{k})}{\partial k} \chi \right)_{k,s} \cdot \mathbf{k} \Theta, \quad (\text{A22})$$

where $\Theta = \Theta[E_{\text{Fermi}} - e(\mathbf{k})]$. Eqs. A20, A21, and A22 can be simplified because $e(k)$ is independent of the spin label, s . Since $e(k)$ is independent of s , the ADM momentum states are two-fold degenerate due to the possibility of an ADM particle having spin $\pm 1/2$. Therefore, we can replace \sum_s with a degeneracy factor of 2. Furthermore, since $e(\mathbf{k})$ depends on only on $|\mathbf{k}|$, the integration over the momentum states is spherically symmetric and the integration can be simplified. After applying these two simplifications and using the normalization of $(\chi^\dagger \chi)_{\mathbf{k},s} = 1$, we now have

$$\langle \chi^\dagger \chi \rangle = \frac{2}{(2\pi^2)^3} \int_0^{k_{\text{F},\chi}} 4\pi dk = \frac{k_{\text{F},\chi}^3}{3\pi^2} = n_\chi \quad (\text{A23})$$

$$\langle \chi^\dagger k_0 \chi \rangle = \frac{1}{\pi^2} \int_0^{k_{\text{F},\chi}} k^2 \sqrt{k^2 + m_\chi^2} dk + g_\chi \phi_0 n_\chi \quad (\text{A24})$$

$$\frac{1}{3} \langle \bar{\chi} \boldsymbol{\gamma} \cdot \mathbf{k} \chi \rangle = \frac{1}{3\pi^2} \int_0^{k_{\text{F},\chi}} \frac{k^4}{\sqrt{k^2 + m_\chi^2}} dk. \quad (\text{A25})$$

where $k_{\text{F},\chi}$ is the ADM Fermi momentum and we have dropped $\Theta[E_{\text{Fermi}} - e(\mathbf{k})]$ because it is equal to 1 between the bounds of integration.

Finally, by inserting the results of Eqs. A4, A23, A24, and A25 into the stress energy tensor components corresponding to the ADM energy density and pressure, the ADM EoS is given by

$$\epsilon_\chi = \frac{1}{\pi^2} \int_0^{k_{\text{F},\chi}} k^2 \sqrt{k^2 + m_\chi^2} dk + \frac{g_\chi^2}{2m_\phi^2} n_\chi^2 \quad (\text{A26})$$

$$p_\chi = \frac{1}{3\pi^2} \int_0^{k_{\text{F},\chi}} \frac{k^4}{\sqrt{k^2 + m_\chi^2}} dk + \frac{g_\chi^2}{2m_\phi^2} n_\chi^2. \quad (\text{A27})$$

Upon integrating the first terms in Eqs. A26 and A27, and restoring \hbar and c , we obtain Eqs. 12 and 13.

Appendix B: Approximating $g_\chi/m_\phi = 0 \text{ MeV}^{-1}$

In order to capture the physically allowed parameter space of the effective fermionic self-repulsion strength, $g_\chi/m_\phi = 0 \text{ MeV}^{-1}$ must be considered. However, since we have assumed $g_B \ll g_\chi$ (see Sec. III C), a non-zero approximation of $g_\chi/m_\phi = 0 \text{ MeV}^{-1}$ is necessary. Here

we approximate zero self-repulsion strength by calculating the average relative radial percent difference (RRPD) between the mass-radius curves of zero self-repulsion and a non-zero self-repulsion strength, which we take to be 10^{-5} MeV^{-1} , for all neutron star masses $\geq 1 M_\odot$. We define the RRPD at a fixed neutron star mass as

$$\text{RRPD} = \frac{|R_{-5} - R_0|}{R_0} \cdot 100, \quad (\text{B1})$$

where R_{-5} is the radius of the neutron star produced by $g_\chi/m_\phi = 10^{-5} \text{ MeV}^{-1}$ and R_0 is the radius of the neutron star produced by zero self-repulsion strength.

To calculate the average RRPD values between the mass-radius relations with zero self-repulsion and $g_\chi/m_\phi = 10^{-5} \text{ MeV}^{-1}$ in a given interval of m_χ and F_χ for a fixed baryonic EoS, we adopt the following procedure. First, we compute the entire mass-radius relation for both $g_\chi/m_\phi = 10^{-5} \text{ MeV}^{-1}$ and $g_\chi/m_\phi = 0 \text{ MeV}^{-1}$ for fixed m_χ and F_χ . Second, we linearly interpolate both mass-radius relations to obtain $R(M)$, i.e., neutron star radius as a function of gravitational mass. With $R(M)$ in-hand, a direct comparison of identical masses between both mass-radius relations can be made. Third, we draw 20 evenly spaced masses from $1 M_\odot$ to the maximum mass of the two mass-radius curves and compute the RRPD for all 20 masses. Fourth, we average over the RRPD values of all masses $> 1 M_\odot$ and save the average value. Finally, steps 1-4 are repeated until the averaged RRPD value of each combination of m_χ and F_χ is obtained.

Using the above procedure to calculate the average RRPD values between $g_\chi/m_\phi = 0 \text{ MeV}^{-1}$ and $g_\chi/m_\phi = 10^{-5} \text{ MeV}^{-1}$, we compute the average RRPD for ADM particle masses within $m_\chi \in [400, 4500] \text{ MeV}$ and ADM mass-fractions within $F_\chi \in [0, 3] \%$. The interval on F_χ was chosen such that it extends through and beyond the ADM mass-fraction prior space defined in Sec. III C. The lower bound on the ADM particle mass interval was determined such that no ADM halo configurations were produced for neutron stars with mass $> 1 M_\odot$ with $F_\chi = 3\%$ and $g_\chi/m_\phi = 0 \text{ MeV}^{-1}$, which ensures only ADM cores will be accounted for all $F_\chi \in [0, 3]\%$. Moreover, the upper bound of $m_\chi = 4500 \text{ MeV}$ was calculated by determining the largest ADM particle mass such that the maximum mass was at least $1 M_\odot$ for $F_\chi = 3\%$ and $g_\chi/m_\phi = 0 \text{ MeV}^{-1}$. Adopting the upper bound of the ADM particle mass interval to be $m_\chi = 4500 \text{ MeV}$ captures the physically relevant ADM core configurations because our Bayesian analysis framework assigns all neutron stars with masses $< 1 M_\odot$ a zero likelihood evaluation.

In Fig. 7 we show the RRPD distribution between the mass-radius relations of zero self-repulsion and $g_\chi/m_\phi = 10^{-5} \text{ MeV}^{-1}$ for three representative baryonic EoSs, each of varying stiffness (top left panel), in the $m_\chi - F_\chi$ plane. For each baryonic EoS, we have spaced each ADM particle mass by $\Delta m_\chi = 250 \text{ MeV}$ and each mass-fraction by $\Delta F_\chi = 0.1\%$ because, when all other EoS parameters are held fixed, both Δm_χ and ΔF_χ have a small

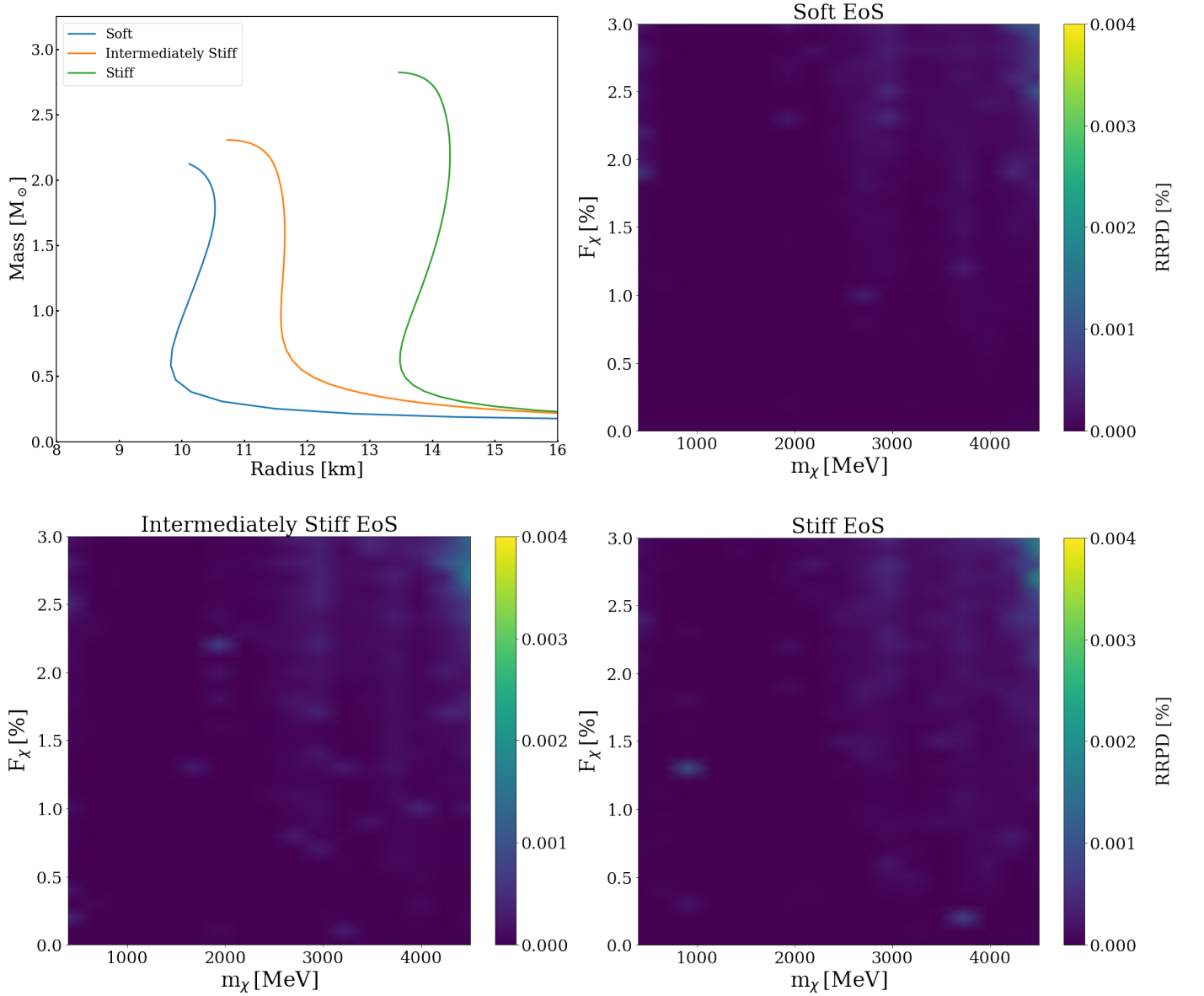


FIG. 7: Top Left: The three underlying baryonic mass-radius curves of varying stiffness from soft (blue) to intermediately stiff (orange) to stiff (green) used in the remaining three panels, respectively; Top Right: Color plot of the RRPD between $g_\chi/m_\phi = 0 \text{ MeV}^{-1}$ and $g_\chi/m_\phi = 10^{-5} \text{ MeV}^{-1}$ in the ADM mass-fraction and particle mass plane for the Soft baryonic EoS; Bottom Left: Same as the top right panel, but for the intermediately stiff baryonic EoS; Bottom right: Same as the top right panel, but for the stiff baryonic EoS. For the top right panel and the bottom two panels, the RRPD values do not exceed 0.004%.

overall effect on the resulting mass-radius relation between each respective step. Although the RRPD distribution is different between each of the baryonic EoSs using Δm_χ and ΔF_χ , the maximum RRPD value is $4 \cdot 10^{-3}\%$ for the soft, intermediately stiff, and stiff baryonic EoSs. Therefore from this observation, we conclude that $g_\chi/m_\phi = 10^{-5} \text{ MeV}^{-1}$ is a sufficient approximation for $g_\chi/m_\phi = 0 \text{ MeV}^{-1}$, regardless of the baryonic EoS, because the maximum RRPD value is $4 \cdot 10^{-3}\%$ which is several orders of magnitude below the observational un-

certainties of neutron star radii considered in this work.

Fig. 8 shows the RRPD distribution between the mass-radius relations of $g_\chi/m_\phi = 0 \text{ MeV}^{-1}$ and $g_\chi/m_\phi = 10^{-5} \text{ MeV}^{-1}$ in which the step size between ADM particle mass points (Δm_χ) and ADM mass-fractions (ΔF_χ) is reduced. Note, we fix the underlying baryonic EoS to be the intermediately stiff EoS from Fig. 7. Reducing the ADM particle mass and mass-fraction step sizes will impact the overall mass-radius relation less between each successive step, thus allowing for better interpolations

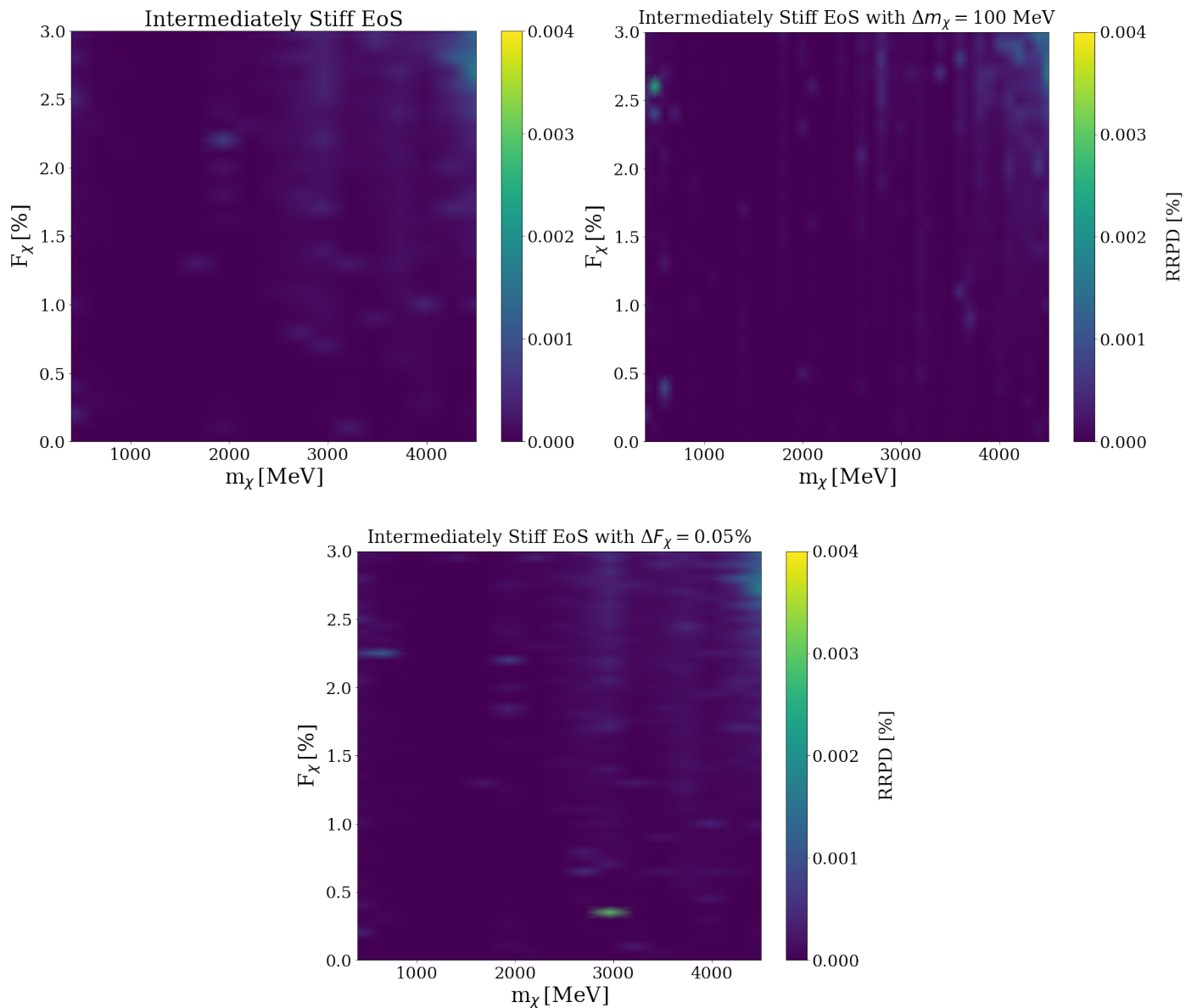


FIG. 8: Top Left: RRPD color plot in the ADM mass-fraction and particle mass plane for the intermediately stiff EoS; Top Right: Same as the top left panel, but the step size along the m_χ axis is changed from 250 MeV to 100 MeV; Bottom: Same as the top left panel, but the step size along the F_χ axis is changed from 0.1% to 0.05%. For all three panels, the maximum RRPD value does not exceed 0.004%.

between grid points in the $m_\chi - F_\chi$ plane. An improved interpolation between (m_χ, F_χ) grid points will allow for the dependency of the RRPD distribution on the grid spacing to be determined. Here we have reduced Δm_χ from 250 MeV to 100 MeV (top right panel) and ΔF_χ from 0.1% to 0.05% (bottom left panel). Fig. 8, shows that for both cases in which we set $\Delta m_\chi = 100$ MeV and $\Delta F_\chi = 0.05\%$, the maximum RRPD value remains below $4 \cdot 10^{-3}\%$. From this observation, we find that the RRPD values are insensitive to variations in Δm_χ and ΔF_χ .

Finally, based on all of the previous observations, we conclude that $g_\chi/m_\phi = 10^{-5} \text{ MeV}^{-1}$ is an adequate approximation to 0 MeV^{-1} within the interval of $m_\chi \in [400, 4500] \text{ MeV}$ and $F_\chi \in [0, 3] \%$, regardless of the choice of Δm_χ , ΔF_χ , and baryonic EoS.

- [1] K. Hebeler, J. M. Lattimer, C. J. Pethick, and A. Schwenk. Equation of State and Neutron Star Properties Constrained by Nuclear Physics and Observation. *Astrophys. J.*, 773(1):11, August 2013. doi:10.1088/0004-637X/773/1/11.
- [2] M. Oertel, M. Hempel, T. Klähn, and S. Typel. Equations of state for supernovae and compact stars. *Rev. Mod. Phys.*, 89:015007, Mar 2017. doi:10.1103/RevModPhys.89.015007.
- [3] M. E. Caplan, A. S. Schneider, and C. J. Horowitz. Elasticity of Nuclear Pasta. *Phys. Rev. Lett.*, 121(13):132701, September 2018. doi:10.1103/PhysRevLett.121.132701.
- [4] L. Tolos and L. Fabbietti. Strangeness in nuclei and neutron stars. *Progress in Particle and Nuclear Physics*, 112:103770, May 2020. doi:10.1016/j.ppnp.2020.103770.
- [5] G.F. Burgio, H.-J. Schulze, I. Vidaña, and J.-B. Wei. Neutron stars and the nuclear equation of state. *Progress in Particle and Nuclear Physics*, 120:103879, 2021. ISSN 0146-6410. doi:https://doi.org/10.1016/j.ppnp.2021.103879.
- [6] Ming-Zhe Han, Yong-Jia Huang, Shao-Peng Tang, and Yi-Zhong Fan. Plausible presence of new state in neutron stars with masses above 0.98MTOV. *Science Bulletin*, 68(9):913–919, May 2023. doi:10.1016/j.scib.2023.04.007.
- [7] J. Keller, K. Hebeler, C. J. Pethick, and A. Schwenk. Neutron Star Matter as a Dilute Solution of Protons in Neutrons. *Phys. Rev. Lett.*, 132(23):232701, June 2024. doi:10.1103/PhysRevLett.132.232701.
- [8] Lee Lindblom. Determining the Nuclear Equation of State from Neutron-Star Masses and Radii. *Astrophys. J.*, 398:569, October 1992. doi:10.1086/171882.
- [9] Anna L. Watts. Constraining the neutron star equation of state using pulse profile modeling. In *Xiamen-CUSTIPEN Workshop on the Equation of State of Dense Neutron-Rich Matter in the Era of Gravitational Wave Astronomy*, volume 2127 of *American Institute of Physics Conference Series*, page 020008, July 2019. doi:10.1063/1.5117798.
- [10] Slavko Bogdanov, Frederick K. Lamb, Simin Mahmoodifar, M. Coleman Miller, Sharon M. Morsink, Thomas E. Riley, Tod E. Strohmayer, Albert K. Tung, Anna L. Watts, Alexander J. Dittmann, Deepto Chakrabarty, Sebastien Guillot, Zaven Arzoumanian, and Keith C. Gendreau. Constraining the Neutron Star Mass-Radius Relation and Dense Matter Equation of State with NICER. II. Emission from Hot Spots on a Rapidly Rotating Neutron Star. *The Astrophysical Journal Letters*, 887(1):L26, December 2019. doi:10.3847/2041-8213/ab5968.
- [11] Slavko Bogdanov, Alexander J. Dittmann, Wynn C. G. Ho, Frederick K. Lamb, Simin Mahmoodifar, M. Coleman Miller, Sharon M. Morsink, Thomas E. Riley, Tod E. Strohmayer, Anna L. Watts, Devarshi Choudhury, Sebastien Guillot, Alice K. Harding, Paul S. Ray, Zorawar Wadiasingh, Michael T. Wolff, Craig B. Markwardt, Zaven Arzoumanian, and Keith C. Gendreau. Constraining the Neutron Star Mass-Radius Relation and Dense Matter Equation of State with NICER. III. Model Description and Verification of Parameter Estimation Codes. *The Astrophysical Journal Letters*, 914(1):L15, June 2021. doi:10.3847/2041-8213/abfb79.
- [12] Keith C. Gendreau, Zaven Arzoumanian, Phillip W. Adkins, Cheryl L. Albert, John F. Anders, Andrew T. Aylward, Charles L. Baker, Erin R. Balsamo, William A. Bamford, Suyog S. Benegalrao, Daniel L. Berry, Shiraz Bhalwani, J. Kevin Black, Carl Blaurock, Ginger M. Bronke, Gary L. Brown, Jason G. Budinoff, Jeffrey D. Cantwell, Thoniel Cazeau, Philip T. Chen, Thomas G. Clement, Andrew T. Colangelo, Jerry S. Coleman, Jonathan D. Cooper-Smith, William E. Dehaven, John P. Doty, Mark D. Egan, Teruaki Enoto, Terry W. Fan, Deneen M. Ferro, Richard Foster, Nicholas M. Galassi, Luis D. Gallo, Chris M. Green, Dave Grosh, Kong Q. Ha, Monther A. Hasouneh, Kristofer B. Heefner, Phyllis Hestnes, Lisa J. Hoge, Tawanda M. Jacobs, John L. Jørgensen, Michael A. Kaiser, James W. Kellogg, Steven J. Kenyon, Richard G. Koenecke, Robert P. Kozon, Beverly LaMarr, Mike D. Lambertson, Anne M. Larson, Steven Lentine, Jesse H. Lewis, Michael G. Lilly, Kuochia Alice Liu, Andrew Malonis, Sridhar S. Manthripragada, Craig B. Markwardt, Bryan D. Matonak, Isaac E. Mcginnis, Roger L. Miller, Alissa L. Mitchell, Jason W. Mitchell, Jelila S. Mohammed, Charles A. Monroe, Kristina M. Montt de Garcia, Peter D. Mulé, Louis T. Nagao, Son N. Ngo, Eric D. Norris, Dwight A. Norwood, Joseph Novotka, Takashi Okajima, Lawrence G. Olsen, Chimaobi O. Onyechu, Henry Y. Orosco, Jacqualine R. Peterson, Kristina N. Pevear, Karen K. Pham, Sue E. Pollard, John S. Pope, Daniel F. Powers, Charles E. Powers, Samuel R. Price, Gregory Y. Prigozhin, Julian B. Ramirez, Winston J. Reid, Ronald A. Remillard, Eric M. Rogstad, Glenn P. Rosecrans, John N. Rowe, Jennifer A. Sager, Claude A. Sanders, Bruce Savadkin, Maxine R. Saylor, Alexander F. Schaeffer, Nancy S. Schweiss, Sean R. Semper, Peter J. Serlemitsos, Larry V. Shackelford, Yang Soong, Jonathan Struebel, Michael L. Vezie, Joel S. Villasenor, Luke B. Winternitz, George I. Wofford, Michael R. Wright, Mike Y. Yang, and Wayne H. Yu. The Neutron star Interior Composition Explorer (NICER): design and development. In Jan-Willem A. den Herder, Tadayuki Takahashi, and Marshall Bautz, editors, *Space Telescopes and Instrumentation 2016: Ultraviolet to Gamma Ray*, volume 9905 of *Society of Photo-Optical Instrumentation Engineers (SPIE) Conference Series*, page 99051H, July 2016. doi:10.1117/12.2231304.
- [13] E. Fonseca, H. T. Cromartie, T. T. Pennucci, P. S. Ray, A. Yu. Kirichenko, S. M. Ransom, P. B. Demorest, I. H. Stairs, Z. Arzoumanian, L. Guillemot, A. Parthasarathy, M. Kerr, I. Cognard, P. T. Baker, H. Blumer, P. R. Brook, M. DeCesar, T. Dolch, F. A. Dong, E. C. Ferrara, W. Fiore, N. Garver-Daniels, D. C. Good, R. Jennings, M. L. Jones, V. M. Kaspi, M. T. Lam, D. R. Lorimer, J. Luo, A. McEwen, J. W. McKee, M. A. McLaughlin, N. McManis, B. W. Meyers, A. Naidu, C. Ng, D. J. Nice, N. Pol, H. A. Radovan, B. Shapiro-Albert, C. M. Tan, S. P. Tendulkar, J. K. Swiggum, H. M. Wahl, and W. W. Zhu. Refined Mass and Geometric Measurements of the High-mass PSR

- J0740+6620. *The Astrophysical Journal Letters*, 915(1):L12, July 2021. doi:10.3847/2041-8213/ac03b8.
- [14] Thomas E. Riley, Anna L. Watts, Paul S. Ray, Slavko Bogdanov, Sebastien Guillot, Sharon M. Morsink, Anna V. Bilous, Zaven Arzoumanian, Devarshi Choudhury, Julia S. Deneva, Keith C. Gendreau, Alice K. Harding, Wynn C. G. Ho, James M. Lattimer, Michael Loewenstein, Renee M. Ludlam, Craig B. Markwardt, Takashi Okajima, Chanda Prescod-Weinstein, Ronald A. Remillard, Michael T. Wolff, Emmanuel Fonseca, H. Thankful Cromartie, Matthew Kerr, Timothy T. Pennucci, Aditya Parthasarathy, Scott Ransom, Ingrid Stairs, Lucas Guillemot, and Ismael Cognard. A NICER View of the Massive Pulsar PSR J0740+6620 Informed by Radio Timing and XMM-Newton Spectroscopy. *The Astrophysical Journal Letters*, 918(2):L27, September 2021. doi:10.3847/2041-8213/ac0a81.
- [15] M. C. Miller, F. K. Lamb, A. J. Dittmann, S. Bogdanov, Z. Arzoumanian, K. C. Gendreau, S. Guillot, W. C. G. Ho, J. M. Lattimer, M. Loewenstein, S. M. Morsink, P. S. Ray, M. T. Wolff, C. L. Baker, T. Cazeau, S. Manthripragada, C. B. Markwardt, T. Okajima, S. Pollard, I. Cognard, H. T. Cromartie, E. Fonseca, L. Guillemot, M. Kerr, A. Parthasarathy, T. T. Pennucci, S. Ransom, and I. Stairs. The Radius of PSR J0740+6620 from NICER and XMM-Newton Data. *The Astrophysical Journal Letters*, 918(2):L28, September 2021. doi:10.3847/2041-8213/ac089b.
- [16] Tuomo Salmi, Serena Vinciguerra, Devarshi Choudhury, Thomas E. Riley, Anna L. Watts, Ronald A. Remillard, Paul S. Ray, Slavko Bogdanov, Sebastien Guillot, Zaven Arzoumanian, Cecilia Chirenti, Alexander J. Dittmann, Keith C. Gendreau, Wynn C. G. Ho, M. Coleman Miller, Sharon M. Morsink, Zorawar Wadiasingh, and Michael T. Wolff. The Radius of PSR J0740+6620 from NICER with NICER Background Estimates. *Astrophys. J.*, 941(2):150, December 2022. doi:10.3847/1538-4357/ac983d.
- [17] Tuomo Salmi, Devarshi Choudhury, Yves Kini, Thomas E. Riley, Serena Vinciguerra, Anna L. Watts, Michael T. Wolff, Zaven Arzoumanian, Slavko Bogdanov, Deepto Chakrabarty, Keith Gendreau, Sebastien Guillot, Wynn C. G. Ho, Daniela Huppenkothen, Renee M. Ludlam, Sharon M. Morsink, and Paul S. Ray. The Radius of the High Mass Pulsar PSR J0740+6620 With 3.6 Years of NICER Data. *arXiv e-prints*, art. arXiv:2406.14466, June 2024. doi:10.48550/arXiv.2406.14466.
- [18] T. E. Riley, A. L. Watts, S. Bogdanov, P. S. Ray, R. M. Ludlam, S. Guillot, Z. Arzoumanian, C. L. Baker, A. V. Bilous, D. Chakrabarty, K. C. Gendreau, A. K. Harding, W. C. G. Ho, J. M. Lattimer, S. M. Morsink, and T. E. Strohmayer. A NICER View of PSR J0030+0451: Millisecond Pulsar Parameter Estimation. *The Astrophysical Journal Letters*, 887(1):L21, December 2019. doi:10.3847/2041-8213/ab481c.
- [19] M. C. Miller, F. K. Lamb, A. J. Dittmann, S. Bogdanov, Z. Arzoumanian, K. C. Gendreau, S. Guillot, A. K. Harding, W. C. G. Ho, J. M. Lattimer, R. M. Ludlam, S. Mahmoodifar, S. M. Morsink, P. S. Ray, T. E. Strohmayer, K. S. Wood, T. Enoto, R. Foster, T. Okajima, G. Prigozhin, and Y. Soong. PSR J0030+0451 Mass and Radius from NICER Data and Implications for the Properties of Neutron Star Matter. *The Astrophysical Journal Letters*, 887(1):L24, December 2019. doi:10.3847/2041-8213/ab50c5.
- [20] Serena Vinciguerra, Tuomo Salmi, Anna L. Watts, Devarshi Choudhury, Thomas E. Riley, Paul S. Ray, Slavko Bogdanov, Yves Kini, Sebastien Guillot, Deepto Chakrabarty, Wynn C. G. Ho, Daniela Huppenkothen, Sharon M. Morsink, Zorawar Wadiasingh, and Michael T. Wolff. An Updated Mass-Radius Analysis of the 2017-2018 NICER Data Set of PSR J0030+0451. *Astrophys. J.*, 961(1):62, January 2024. doi:10.3847/1538-4357/acfb83.
- [21] Devarshi Choudhury, Tuomo Salmi, Serena Vinciguerra, Thomas E. Riley, Yves Kini, Anna L. Watts, Bas Dorsman, Slavko Bogdanov, Sebastien Guillot, Paul S. Ray, Daniel J. Reardon, Ronald A. Remillard, Anna V. Bilous, Daniela Huppenkothen, James M. Lattimer, Nathan Rutherford, Zaven Arzoumanian, Keith C. Gendreau, Sharon M. Morsink, and Wynn C. G. Ho. A NICER View of the Nearest and Brightest Millisecond Pulsar: PSR J0437-4715. *The Astrophysical Journal Letters*, 971(1):L20, August 2024. doi:10.3847/2041-8213/ad5a6f.
- [22] Daniel J. Reardon, Matthew Bailes, Ryan M. Shannon, Chris Flynn, Jacob Askew, N. D. Ramesh Bhat, Zucheng Chen, Malgorzata Curylo, Yi Feng, George B. Hobbs, Agastya Kapur, Matthew Kerr, Xiaojin Liu, Richard N. Manchester, Rami Mandow, Saurav Mishra, Christopher J. Russell, Mohsen Shamohammadi, Lei Zhang, and Andrew Zic. The Neutron Star Mass, Distance, and Inclination from Precision Timing of the Brilliant Millisecond Pulsar J0437-4715. *The Astrophysical Journal Letters*, 971(1):L18, August 2024. doi:10.3847/2041-8213/ad614a.
- [23] G. Raaijmakers, T. E. Riley, A. L. Watts, S. K. Greif, S. M. Morsink, K. Hebeler, A. Schwenk, T. Hinderer, S. Nissanke, S. Guillot, Z. Arzoumanian, S. Bogdanov, D. Chakrabarty, K. C. Gendreau, W. C. G. Ho, J. M. Lattimer, R. M. Ludlam, and M. T. Wolff. A Nicer View of PSR J0030+0451: Implications for the Dense Matter Equation of State. *Astrophysical Journal Letters*, 887(1):L22, December 2019. doi:10.3847/2041-8213/ab451a.
- [24] G. Raaijmakers, S. K. Greif, T. E. Riley, T. Hinderer, K. Hebeler, A. Schwenk, A. L. Watts, S. Nissanke, S. Guillot, J. M. Lattimer, and R. M. Ludlam. Constraining the Dense Matter Equation of State with Joint Analysis of NICER and LIGO/Virgo Measurements. *Astrophysical Journal Letters*, 893(1):L21, April 2020. doi:10.3847/2041-8213/ab822f.
- [25] G. Raaijmakers, S. K. Greif, K. Hebeler, T. Hinderer, S. Nissanke, A. Schwenk, T. E. Riley, A. L. Watts, J. M. Lattimer, and W. C. G. Ho. Constraints on the Dense Matter Equation of State and Neutron Star Properties from NICER’s Mass-Radius Estimate of PSR J0740+6620 and Multimessenger Observations. *The Astrophysical Journal Letters*, 918(2):L29, September 2021. doi:10.3847/2041-8213/ac089a.
- [26] Jia Jie Li, Armen Sedrakian, and Mark Alford. Relativistic hybrid stars in light of the NICER PSR J 0740 +6620 radius measurement. *Phys. Rev. D*, 104(12):L121302, December 2021. doi:10.1103/PhysRevD.104.L121302.
- [27] Isaac Legred, Katerina Chatziioannou, Reed Essick, Sophia Han, and Philippe Landry. Impact of the PSR J

- 0740 +6620 radius constraint on the properties of high-density matter. *Phys. Rev. D*, 104(6):063003, September 2021. doi:10.1103/PhysRevD.104.063003.
- [28] Peter T. H. Pang, Ingo Tews, Michael W. Coughlin, Mattia Bulla, Chris Van Den Broeck, and Tim Dietrich. Nuclear Physics Multimessenger Astrophysics Constraints on the Neutron Star Equation of State: Adding NICER’s PSR J0740+6620 Measurement. *Astrophys. J.*, 922(1):14, November 2021. doi:10.3847/1538-4357/ac19ab.
- [29] Shao-Peng Tang, Jin-Liang Jiang, Ming-Zhe Han, Yi-Zhong Fan, and Da-Ming Wei. Constraints on the phase transition and nuclear symmetry parameters from PSR J 0740 +6620 and multimessenger data of other neutron stars. *Phys. Rev. D*, 104(6):063032, September 2021. doi:10.1103/PhysRevD.104.063032.
- [30] Eemeli Annala, Tyler Gorda, Evangelia Katerini, Aleks Kurkela, Joonas Nättilä, Vasileios Paschalidis, and Aleks Vuorinen. Multimessenger Constraints for Ultradense Matter. *Physical Review X*, 12(1):011058, January 2022. doi:10.1103/PhysRevX.12.011058.
- [31] Bhaskar Biswas. Bayesian Model Selection of Neutron Star Equations of State Using Multi-messenger Observations. *Astrophys. J.*, 926(1):75, February 2022. doi:10.3847/1538-4357/ac447b.
- [32] Nathan Rutherford, Melissa Mendes, Isak Svensson, Achim Schwenk, Anna L. Watts, Kai Hebeler, Jonas Keller, Chanda Prescod-Weinstein, Devarshi Choudhury, Geert Raaijmakers, Tuomo Salmi, Patrick Timmerman, Serena Vinciguerra, Sebastien Guillot, and James M. Lattimer. Constraining the Dense Matter Equation of State with New NICER Mass–Radius Measurements and New Chiral Effective Field Theory Inputs. *The Astrophysical Journal Letters*, 971(1):L19, August 2024. doi:10.3847/2041-8213/ad5f02.
- [33] Chun Huang, Geert Raaijmakers, Anna L. Watts, Laura Tolos, and Constança Providência. Constraining a relativistic mean field model using neutron star mass-radius measurements I: nucleonic models. *Monthly Notices of the RAS*, 529(4):4650–4665, April 2024. doi:10.1093/mnras/stae844.
- [34] J. Keller, K. Hebeler, and A. Schwenk. Nuclear equation of state for arbitrary proton fraction and temperature based on chiral effective field theory and a gaussian process emulator. *Phys. Rev. Lett.*, 130:072701, Feb 2023. doi:10.1103/PhysRevLett.130.072701.
- [35] Anna L. Watts, WenFei Yu, Juri Poutanen, Shu Zhang, Sudip Bhattacharyya, Slavko Bogdanov, Long Ji, Alessandro Patruno, Thomas E. Riley, Pavel Bakala, Altan Baykal, Federico Bernardini, Ignazio Bombaci, Edward Brown, Yuri Cavecchi, Deepto Chakrabarty, Jérôme Chenevez, Nathalie Degenaar, Melania Del Santo, Tiziana Di Salvo, Victor Doroshenko, Maurizio Falanga, Robert D. Ferdman, Marco Feroci, Angelo F. Gambino, MingYu Ge, Svenja K. Greif, Sebastien Guillot, Can Gungor, Dieter H. Hartmann, Kai Hebeler, Alexander Heger, Jeroen Homan, Rosario Iaria, Jean in’t. Zand, Oleg Kargaltsev, Aleks Kurkela, XiaoYu Lai, Ang Li, XiangDong Li, ZhaoSheng Li, Manuel Linares, FangJun Lu, Simin Mahmoodifar, Mariano Méndez, M. Coleman Miller, Sharon Morsink, Joonas Nättilä, Andrea Possenti, Chanda Prescod-Weinstein, JinLu Qu, Alessandro Riggio, Tuomo Salmi, Andrea Sanna, Andrea Santangelo, Hendrik Schatz, Achim Schwenk, LiMing Song, Eva Šrámková, Benjamin Stappers, Holger Stiele, Tod Strohmayer, Ingo Tews, Laura Tolos, Gabriel Török, David Tsang, Martin Urbanec, Andrea Vacchi, RenXin Xu, YuPeng Xu, Silvia Zane, GuoBao Zhang, ShuangNan Zhang, WenDa Zhang, ShiJie Zheng, and Xia Zhou. Dense matter with eXTP. *Science China Physics, Mechanics, and Astronomy*, 62(2):29503, February 2019. doi:10.1007/s11433-017-9188-4.
- [36] Paul S. Ray, Zaven Arzoumanian, David Ballantyne, Enrico Bozzo, Soren Brandt, Laura Brenneman, Deepto Chakrabarty, Marc Christophersen, Alessandro DeRosa, Marco Feroci, Keith Gendreau, Adam Goldstein, Dieter Hartmann, Margarita Hernanz, Peter Jenke, Erin Kara, Tom Maccarone, Michael McDonald, Michael Nowak, Bernard Philips, Ron Remillard, Abigail Stevens, John Tomsick, Anna Watts, Colleen Wilson-Hodge, Kent Wood, Silvia Zane, Marco Ajello, Will Alston, Diego Altamirano, Vallia Antoniou, Kavitha Arur, Dominic Ashton, Katie Auchettl, Tom Ayres, Matteo Bachetti, Mislav Balokovic, Matthew Baring, Altan Baykal, Mitch Begelman, Narayana Bhat, Slavko Bogdanov, Michael Briggs, Esra Bulbul, Petrus Bult, Eric Burns, Ed Cackett, Riccardo Campana, Amir Caspi, Yuri Cavecchi, Jerome Chenevez, Mike Cherry, Robin Corbet, Michael Corcoran, Alessandra Corsi, Nathalie Degenaar, Jeremy Drake, Steve Eikenberry, Teruaki Enoto, Chris Fragile, Felix Fuerst, Poshak Gandhi, Javier Garcia, Adam Goldstein, Anthony Gonzalez, Brian Grefenstette, Victoria Grinberg, Bruce Grossan, Sebastien Guillot, Tolga Guver, Daryl Haggard, Craig Heinke, Sebastian Heinz, Paul Hemphill, Jeroen Homan, Michelle Hui, Daniela Huppenkothen, Adam Ingram, Jimmy Irwin, Gaurava Jaisawal, Amruta Jaodand, Emrah Kalemci, David Kaplan, Laurens Keek, Jamie Kennea, Matthew Kerr, Michiel van der Klis, Daniel Kocevski, Mike Koss, Adam Kowalski, Dong Lai, Fred Lamb, Silas Laycock, Joseph Lazio, Davide Lazzati, Dana Longcope, Michael Loewenstein, Dipankair Maitra, Walid Majid, W. Peter Maksym, Christian Malacaria, Raffaella Margutti, Adrian Martindale, Ian McHardy, Manuel Meyer, Matt Middleton, Jon Miller, Cole Miller, Sara Motta, Joey Neilsen, Tommy Nelson, Scott Noble, Paul O’Brien, Julian Osborne, Rachel Osten, Feryal Ozel, Nipuni Palliyaguru, Dheeraj Pasham, Alessandro Patruno, Vero Pelassa, Maria Petropoulou, Maura Pilia, Martin Pohl, David Pooley, Chanda Prescod-Weinstein, Dimitrios Psaltis, Geert Raaijmakers, Chris Reynolds, Thomas E. Riley, Greg Salvesen, Andrea Santangelo, Simone Scaringi, Stephane Schanne, Jeremy Schnittman, David Smith, Krista Lynne Smith, Bradford Snios, Andrew Steiner, Jack Steiner, Luigi Stella, Tod Strohmayer, Ming Sun, Thomas Tauris, Corbin Taylor, Aaron Tohuavohu, Andrea Vacchi, Georgios Vasilopoulos, Alexandra Vele-dina, Jonelle Walsh, Nevin Weinberg, Dan Wilkins, Richard Willingale, Joern Wilms, Lisa Winter, Michael Wolff, Jean in ’t Zand, Andreas Zezas, Bing Zhang, and Abdu Zoghbi. STROBE-X: X-ray Timing and Spectroscopy on Dynamical Timescales from Microseconds to Years. *arXiv e-prints*, art. arXiv:1903.03035, Mar 2019.
- [37] Kirpal Nandra, Didier Barret, Xavier Barcons, Andy Fabian, Jan-Willem den Herder, Luigi Piro,

- Mike Watson, Christophe Adami, James Aird, Jose Manuel Afonso, Dave Alexander, Costanza Argiroffi, Lorenzo Amati, Monique Arnaud, Jean-Luc Atteia, Marc Audard, Carles Badenes, Jean Ballet, Lucia Ballo, Aya Bamba, Anil Bhardwaj, Elia Stefano Battistelli, Werner Becker, Michaël De Becker, Ehud Behar, Stefano Bianchi, Veronica Biffi, Laura Bîrzan, Fabrizio Bocchino, Slavko Bogdanov, Laurence Boirin, Thomas Boller, Stefano Borgani, Katharina Borm, Nicolas Bouché, Hervé Bourdin, Richard Bower, Valentina Braito, Enzo Branchini, Graziella Branduardi-Raymont, Joel Bregman, Laura Brenne- man, Murray Brightman, Marcus Brüggem, Johannes Buchner, Esra Bulbul, Marcella Brusa, Michal Bursa, Alessandro Caccianiga, Ed Cackett, Sergio Campana, Nico Cappelluti, Massimo Cappi, Francisco Carrera, Maite Ceballos, Finn Christensen, You-Hua Chu, Eugene Churazov, Nicolas Clerc, Stephane Corbel, Amalia Corral, Andrea Comastri, Elisa Costantini, Judith Croston, Mauro Dadina, Antonino D’Ai, Anne Decourchelle, Roberto Della Ceca, Konrad Dennerl, Klaus Dolag, Chris Done, Michal Dovciak, Jeremy Drake, Dominique Eckert, Alastair Edge, Stefano Etori, Yuichiro Ezoe, Eric Feigelson, Rob Fender, Chiara Feruglio, Alexis Finoguenov, Fabrizio Fiore, Massimiliano Galeazzi, Sarah Gallagher, Poshak Gandhi, Massimo Gaspari, Fabio Gastaldello, Antonis Georgakakis, Ioannis Georgantopoulos, Marat Gilfanov, Myriam Gitti, Randy Gladstone, Rene Goosmann, Eric Gosset, Nicolas Grosso, Manuel Guedel, Martin Guerrero, Frank Haberl, Martin Hardcastle, Sebastian Heinz, Almudena Alonso Herrero, Anthony Hervé, Mats Holmstrom, Kazushi Iwasawa, Peter Jonker, Jelle Kaastra, Erin Kara, Vladimir Karas, Joel Kastner, Andrew King, Daria Kosenko, Dimita Koutroumpa, Ralph Kraft, Ingo Kreykenbohm, Rosine Lallement, Giorgio Lanzuisi, J. Lee, Marianne Lemoine-Goumard, Andrew Lobban, Giuseppe Lodato, Lorenzo Lovisari, Simone Lotti, Ian McCharthy, Brian McNamara, Antonio Maggio, Roberto Maiolino, Barbara De Marco, Domitilla de Martino, Silvia Mateos, Giorgio Matt, Ben Maughan, Pasquale Mazzotta, Mariano Mendez, Andrea Merloni, Giuseppina Micela, Marco Miceli, Robert Mignani, Jon Miller, Giovanni Miniutti, Silvano Molendi, Rodolfo Montez, Alberto Moretti, Christian Motch, Yaël Nazé, Jukka Nevalainen, Fabrizio Nicastro, Paul Nulsen, Takaya Ohashi, Paul O’Brien, Julian Osborne, Lida Oskinova, Florian Pacaud, Frederik Paerels, Mat Page, Iossif Papadakis, Giovanni Pareschi, Robert Petre, Pierre-Olivier Petrucci, Enrico Piconcelli, Ignazio Pillitteri, C. Pinto, Jelle de Plaa, Etienne Pointecouteau, Trevor Ponman, Gabriele Ponti, Delphine Porquet, Ken Pounds, Gabriel Pratt, Peter Predehl, Daniel Proga, Dimitrios Psaltis, David Rafferty, Miriam Ramos-Ceja, Piero Ranalli, Elena Rasia, Arne Rau, Gregor Rauw, Nanda Rea, Andy Read, James Reeves, Thomas Reiprich, Matthieu Renaud, Chris Reynolds, Guido Risaliti, Jerome Rodriguez, Paola Rodriguez Hidalgo, Mauro Roncarelli, David Rosario, Mariachiara Rossetti, Agata Rozanska, Emmanouil Rovilos, Ruben Salvaterra, Mara Salvato, Tiziana Di Salvo, Jeremy Sanders, Jorge Sanz-Forcada, Kevin Schawinski, Joop Schaye, Axel Schwöpe, Salvatore Sciortino, Paola Severgnini, Francesco Shankar, Debora Sijacki, Stuart Sim, Christian Schmid, Randall Smith, Andrew Steiner, Beate Stelzer, Gordon Stewart, Tod Strohmayer, Lothar Strüder, Ming Sun, Yoh Takei, V. Tatischeff, Andreas Tiengo, Francesco Tombesi, Ginevra Trinchieri, T. G. Tsuru, Asif Ud-Doula, Eugenio Ursino, Lynne Valencic, Eros Vanzella, Simon Vaughan, Cristian Vignali, Jacco Vink, Fabio Vito, Marta Volonteri, Daniel Wang, Natalie Webb, Richard Willingale, Joern Wilms, Michael Wise, Diana Worrall, Andrew Young, Luca Zampieri, Jean In’t Zand, Silvia Zane, Andreas Zezas, Yuying Zhang, and Irina Zhuravleva. The Hot and Energetic Universe: A White Paper presenting the science theme motivating the Athena+ mission. *arXiv e-prints*, art. arXiv:1306.2307, June 2013. doi:10.48550/arXiv.1306.2307.
- [38] Ann E. Nelson, Sanjay Reddy, and Dake Zhou. Dark halos around neutron stars and gravitational waves. *Journal of Cosmology and Astroparticle Physics*, 2019(7): 012, July 2019. doi:10.1088/1475-7516/2019/07/012.
- [39] V. Sagun, V. Sagun”, E. Giangrandi”, O. Ivanytskyi”, I. Lopes”, and K. Bugaev. Constraints on the fermionic dark matter from observations of neutron stars. In *Particles and Nuclei International Conference 2021*, page 313, April 2022. doi:10.22323/1.380.0313.
- [40] Robin Fynn Diedrichs, Niklas Becker, Cédric Jockel, Jan-Erik Christian, Laura Sagunski, and Jürgen Schaffner-Bielich. Tidal deformability of fermion-boson stars: Neutron stars admixed with ultralight dark matter. *Phys. Rev. D*, 108(6):064009, September 2023. doi: 10.1103/PhysRevD.108.064009.
- [41] Joseph Bramante and Nirmal Raj. Dark matter in compact stars. *Physics Reports*, 1052:1–48, February 2024. doi:10.1016/j.physrep.2023.12.001.
- [42] Zakary Buras-Stubbs and Ilídio Lopes. Bosonic dark matter dynamics in hybrid neutron stars. *Phys. Rev. D*, 109(4):043043, February 2024. doi: 10.1103/PhysRevD.109.043043.
- [43] Atanu Guha and Debashree Sen. Constraining the mass of fermionic dark matter from its feeble interaction with hadronic matter via dark mediators in neutron stars. *Phys. Rev. D*, 109(4):043038, February 2024. doi: 10.1103/PhysRevD.109.043038.
- [44] Cédric Jockel and Laura Sagunski. Fermion Proca Stars: Vector-Dark-Matter-Admixed Neutron Stars. *Particles*, 7(1):52–79, January 2024. doi: 10.3390/particles7010004.
- [45] Shafayat Shawqi and Sharon M. Morsink. Interpreting Mass and Radius Measurements of Neutron Stars with Dark Matter Halos. 6 2024.
- [46] Zhiqiang Miao, Yaofeng Zhu, Ang Li, and Feng Huang. Structure and pulse profiles of dark matter admixed neutron stars. *arXiv e-prints*, art. arXiv:2204.05560, April 2022. Accepted to ApJ.
- [47] Soroush Shakeri and Davood Rafiei Karkevandi. Bosonic dark matter in light of the NICER precise mass-radius measurements. *Phys. Rev. D*, 109(4):043029, February 2024. doi:10.1103/PhysRevD.109.043029.
- [48] Sarah Louisa Pitz and Jürgen Schaffner-Bielich. Generating ultra-compact neutron stars with bosonic dark matter. *arXiv e-prints*, art. arXiv:2408.13157, August 2024. doi:10.48550/arXiv.2408.13157.
- [49] John Ellis, Gert Hütsi, Kristjan Kannike, Luca Marzola, Martti Raidal, and Ville Vaskonen. Dark matter effects on neutron star properties. *Phys. Rev. D*, 97(12):123007,

- June 2018. doi:10.1103/PhysRevD.97.123007.
- [50] O. Ivanytskyi, V. Sagun, and I. Lopes. Neutron stars: New constraints on asymmetric dark matter. *Phys. Rev. D*, 102(6):063028, September 2020. doi: 10.1103/PhysRevD.102.063028.
- [51] Ben Kain. Dark matter admixed neutron stars. *Phys. Rev. D*, 103(4):043009, February 2021. doi: 10.1103/PhysRevD.103.043009.
- [52] Davood Rafiei Karkevandi, Soroush Shakeri, Violetta Sagun, and Oleksii Ivanytskyi. Bosonic dark matter in neutron stars and its effect on gravitational wave signal. *Phys. Rev. D*, 105(2):023001, January 2022. doi: 10.1103/PhysRevD.105.023001.
- [53] Davood Rafiei Karkevandi, Mahboubeh Shahrabaf, Soroush Shakeri, and Stefan Typel. Exploring the Distribution and Impact of Bosonic Dark Matter in Neutron Stars. *Particles*, 7(1):201–213, March 2024. doi: 10.3390/particles7010011.
- [54] Mar Bastero-Gil, Teresa Huertas-Roldan, and Daniel Santos. The neutron decay anomaly, neutron stars and dark matter. *arXiv e-prints*, art. arXiv:2403.08666, March 2024. doi:10.48550/arXiv.2403.08666.
- [55] Domenico Scordino and Ignazio Bombaci. Dark matter admixed neutron stars with a realistic nuclear equation of state from chiral nuclear interactions. *arXiv e-prints*, art. arXiv:2405.19251, May 2024. doi: 10.48550/arXiv.2405.19251.
- [56] Andreas Konstantinou. The Effect of a Dark Matter Core on the Structure of a Rotating Neutron Star. *arXiv e-prints*, art. arXiv:2405.01487, May 2024. doi: 10.48550/arXiv.2405.01487.
- [57] H. C. Das, Ankit Kumar, Bharat Kumar, and Suresh Kumar Patra. Dark Matter Effects on the Compact Star Properties. *Galaxies*, 10(1):14, January 2022. doi:10.3390/galaxies10010014.
- [58] Arpan Das, Tuhin Malik, and Alekha C. Nayak. Dark matter admixed neutron star properties in light of gravitational wave observations: A two fluid approach. *Phys. Rev. D*, 105:123034, Jun 2022. doi: 10.1103/PhysRevD.105.123034.
- [59] Debashree Sen and Atanu Guha. Implications of feebly interacting dark sector on neutron star properties and constraints from GW170817. *Monthly Notices of the RAS*, 504(3):3354–3363, July 2021. doi: 10.1093/mnras/stab1056.
- [60] Atanu Guha and Debashree Sen. Feeble DM-SM interaction via new scalar and vector mediators in rotating neutron stars. *Journal of Cosmology and Astroparticle Physics*, 2021(9):027, September 2021. doi: 10.1088/1475-7516/2021/09/027.
- [61] Edoardo Giangrandi, Violetta Sagun, Oleksii Ivanytskyi, Constança Providência, and Tim Dietrich. The Effects of Self-interacting Bosonic Dark Matter on Neutron Star Properties. *Astrophys. J.*, 953(1):115, 2023. doi:10.3847/1538-4357/ace104.
- [62] Mikel F. Barbat, Jürgen Schaffner-Bielich, and Laura Tolos. A comprehensive study of compact stars with dark matter. *arXiv e-prints*, art. arXiv:2404.12875, April 2024. doi:10.48550/arXiv.2404.12875.
- [63] Hongyi Sun and Dehua Wen. A new criterion for the existence of dark matter in neutron stars. *arXiv e-prints*, art. arXiv:2312.17288, December 2023. doi: 10.48550/arXiv.2312.17288.
- [64] Prashant Thakur, Tuhin Malik, and Tarun Kumar Jha. Towards Uncovering Dark Matter Effects on Neutron Star Properties: A Machine Learning Approach. *Particles*, 7(1):80–95, January 2024. doi: 10.3390/particles7010005.
- [65] Prashant Thakur, Tuhin Malik, Arpan Das, T. K. Jha, and Constança Providência. Exploring robust correlations between fermionic dark matter model parameters and neutron star properties: A two-fluid perspective. *Phys. Rev. D*, 109(4):043030, February 2024. doi: 10.1103/PhysRevD.109.043030.
- [66] Swarnim Shirke, Bikram Keshari Pradhan, Debarati Chatterjee, Laura Sagunski, and Jürgen Schaffner-Bielich. Effects of Dark Matter on f -mode oscillations of Neutron Stars. *arXiv e-prints*, art. arXiv:2403.18740, March 2024. doi:10.48550/arXiv.2403.18740.
- [67] Pratik Thakur, Anil Kumar, Vivek Baruah Thapa, Vishal Parmar, and Monika Sinha. Exploring non-radial oscillation modes in dark matter admixed neutron stars. *arXiv e-prints*, art. arXiv:2406.07470, June 2024. doi: 10.48550/arXiv.2406.07470.
- [68] Suman Pal and Gargi Chaudhuri. Effect of dark matter interaction on hybrid star in the light of the recent astrophysical observations. *arXiv e-prints*, art. arXiv:2405.04856, May 2024. doi: 10.48550/arXiv.2405.04856.
- [69] Mauro Mariani, Conrado Albertus, M. del Rosario Alessandrini, Milva G. Orsaria, M. Ángeles Pérez-García, and Ignacio F. Ranea-Sandoval. Constraining self-interacting fermionic dark matter in admixed neutron stars using multimessenger astronomy. *Monthly Notices of the RAS*, 527(3):6795–6806, January 2024. doi:10.1093/mnras/stad3658.
- [70] Premachand Mahapatra, Chiranjeeb Singha, Ayush Hazarika, and Prasanta Kumar Das. Implications of Fermionic Dark Matter Interactions on Anisotropic Neutron Stars. *arXiv e-prints*, art. arXiv:2408.14020, August 2024. doi:10.48550/arXiv.2408.14020.
- [71] Ankit Kumar and Hajime Sotani. Constraints on the parameter space in dark matter admixed neutron stars. *arXiv e-prints*, art. arXiv:2408.15312, August 2024. doi: 10.48550/arXiv.2408.15312.
- [72] M. Iu. Khlopov, B. A. Malomed, and Ia. B. Zel'dovich. Gravitational instability of scalar fields and formation of primordial black holes. *Monthly Notices of the RAS*, 215:575–589, August 1985. doi: 10.1093/mnras/215.4.575.
- [73] Gianfranco Bertone and Malcolm Fairbairn. Compact stars as dark matter probes. *Phys. Rev. D*, 77(4):043515, February 2008. doi:10.1103/PhysRevD.77.043515.
- [74] Chris Kouvaris and Peter Tinyakov. Constraining asymmetric dark matter through observations of compact stars. *Phys. Rev. D*, 83(8):083512, April 2011. doi: 10.1103/PhysRevD.83.083512.
- [75] Moira I. Gresham and Kathryn M. Zurek. Asymmetric dark stars and neutron star stability. *Phys. Rev. D*, 99(8):083008, April 2019. doi: 10.1103/PhysRevD.99.083008.
- [76] Andreas Bauswein, Gang Guo, Jr. Lien-Hua, Yen-Hsun Lin, and Meng-Ru Wu. Compact dark objects in neutron star mergers. *Phys. Rev. D*, 107(8):083002, April 2023. doi:10.1103/PhysRevD.107.083002.
- [77] Hannes R. Rüter, Violetta Sagun, Wolfgang Tichy, and Tim Dietrich. Quasiequilibrium configurations of bi-

- nary systems of dark matter admixed neutron stars. *Phys. Rev. D*, 108(12):124080, December 2023. doi:10.1103/PhysRevD.108.124080.
- [78] Mattia Emma, Federico Schianchi, Francesco Pannarale, Violetta Sagun, and Tim Dietrich. Numerical Simulations of Dark Matter Admixed Neutron Star Binaries. *Particles*, 5(3):273–286, July 2022. doi:10.3390/particles5030024.
- [79] Rebecca K. Leane and Joshua Tong. Optimal Celestial Bodies for Dark Matter Detection. *arXiv e-prints*, art. arXiv:2405.05312, May 2024. doi:10.48550/arXiv.2405.05312.
- [80] Nathan Rutherford, Geert Raaijmakers, Chanda Prescod-Weinstein, and Anna Watts. Constraining bosonic asymmetric dark matter with neutron star mass-radius measurements. *Phys. Rev. D*, 107(10):103051, May 2023. doi:10.1103/PhysRevD.107.103051.
- [81] Kalliopi Petraki and Raymond R. Volkas. Review of Asymmetric Dark Matter. *International Journal of Modern Physics A*, 28(19):1330028, July 2013. doi:10.1142/S0217751X13300287.
- [82] Kalliopi Petraki, Lauren Pearce, and Alexander Kusenko. Self-interacting asymmetric dark matter coupled to a light massive dark photon. *Journal of Cosmology and Astroparticle Physics*, 2014(7):039, July 2014. doi:10.1088/1475-7516/2014/07/039.
- [83] Sharon M. Morsink, Denis A. Leahy, Coire Cadeau, and John Braga. The Oblate Schwarzschild Approximation for Light Curves of Rapidly Rotating Neutron Stars. *Astrophys. J.*, 663(2):1244–1251, July 2007. doi:10.1086/518648.
- [84] Mohammad AlGendy and Sharon M. Morsink. Universality of the Acceleration due to Gravity on the Surface of a Rapidly Rotating Neutron Star. *Astrophys. J.*, 791(2):78, August 2014. doi:10.1088/0004-637X/791/2/78.
- [85] P. S. Ray, Z. Arzoumanian, S. Brandt, E. Burns, D. Chakrabarty, M. Feroci, K. C. Gendreau, O. Gevin, M. Hernanz, P. Jenke, S. Kenyon, J. L. Gálvez, T. J. Maccarone, T. Okajima, R. A. Remillard, S. Schanne, C. Tenzer, A. Vacchi, C. A. Wilson-Hodge, B. Winter, S. Zane, D. R. Ballantyne, E. Bozzo, L. W. Brenneman, E. Cackett, A. De Rosa, A. Goldstein, D. H. Hartmann, M. McDonald, A. L. Stevens, J. A. Tomsick, A. L. Watts, K. S. Wood, and A. Zoghbi. STROBE-X: a probe-class mission for x-ray spectroscopy and timing on timescales from microseconds to years. In *Space Telescopes and Instrumentation 2018: Ultraviolet to Gamma Ray*, volume 10699 of *Society of Photo-Optical Instrumentation Engineers (SPIE) Conference Series*, page 1069919, July 2018. doi:10.1117/12.2312257.
- [86] Richard C. Tolman. Static Solutions of Einstein’s Field Equations for Spheres of Fluid. *Physical Review*, 55(4):364–373, February 1939. doi:10.1103/PhysRev.55.364.
- [87] J. R. Oppenheimer and G. M. Volkoff. On Massive Neutron Cores. *Physical Review*, 55(4):374–381, February 1939. doi:10.1103/PhysRev.55.374.
- [88] Violetta Sagun, Edoardo Giangrandi, Tim Dietrich, Oleksii Ivanytskyi, Rodrigo Negreiros, and Constança Providência. What Is the Nature of the HESS J1731-347 Compact Object? *Astrophys. J.*, 958(1):49, November 2023. doi:10.3847/1538-4357/acfc9e.
- [89] Fredrik Sandin and Paolo Ciarcelluti. Effects of mirror dark matter on neutron stars. *Astroparticle Physics*, 32(5):278–284, December 2009. doi:10.1016/j.astropartphys.2009.09.005.
- [90] Teresa Marrodán Undagoitia and Ludwig Rauch. Dark matter direct-detection experiments. *Journal of Physics G Nuclear Physics*, 43(1):013001, January 2016. doi:10.1088/0954-3899/43/1/013001.
- [91] Ermal Rrapaj and Sanjay Reddy. Nucleon-nucleon bremsstrahlung of dark gauge bosons and revised supernova constraints. *Phys. Rev. C*, 94(4):045805, October 2016. doi:10.1103/PhysRevC.94.045805.
- [92] Michael Collier, Djuna Croon, and Rebecca K. Leane. Tidal Love numbers of novel and admixed celestial objects. *Phys. Rev. D*, 106(12):123027, December 2022. doi:10.1103/PhysRevD.106.123027.
- [93] S. K. Greif, G. Raaijmakers, K. Hebeler, A. Schwenk, and A. L. Watts. Equation of state sensitivities when inferring neutron star and dense matter properties. *Monthly Notices of the RAS*, 485(4):5363–5376, June 2019. doi:10.1093/mnras/stz654.
- [94] Jocelyn S. Read, Benjamin D. Lackey, Benjamin J. Owen, and John L. Friedman. Constraints on a phenomenologically parametrized neutron-star equation of state. *Phys. Rev. D*, 79(12):124032, June 2009. doi:10.1103/PhysRevD.79.124032.
- [95] Gordon Baym, Christopher Pethick, and Peter Sutherland. The Ground State of Matter at High Densities: Equation of State and Stellar Models. *Astrophys. J.*, 170:299, December 1971. doi:10.1086/151216.
- [96] C. Drischler, J. W. Holt, and C. Wellenhofer. Chiral Effective Field Theory and the High-Density Nuclear Equation of State. *Annual Review of Nuclear and Particle Science*, 71:403–432, September 2021. doi:10.1146/annurev-nucl-102419-041903.
- [97] I. Tews, J. Carlson, S. Gandolfi, and S. Reddy. Constraining the Speed of Sound inside Neutron Stars with Chiral Effective Field Theory Interactions and Observations. *Astrophys. J.*, 860(2):149, June 2018. doi:10.3847/1538-4357/aac267.
- [98] K. Hebeler and A. Schwenk. Chiral three-nucleon forces and neutron matter. *Phys. Rev. C*, 82(1):014314, July 2010. doi:10.1103/PhysRevC.82.014314.
- [99] Geert Raaijmakers, Patrick Timmerman, Nathan Rutherford, Tuomo Salmi, Anna L. Watts, and Chanda Prescod-Weinstein. NEoS-T: A Python package for nested sampling of the neutron star equation of state. *Journal of Open Source Software*, submitted, 2024.
- [100] Chris Kouvaris and Peter Tinyakov. Excluding Light Asymmetric Bosonic Dark Matter. *Phys. Rev. Lett.*, 107(9):091301, August 2011. doi:10.1103/PhysRevLett.107.091301.
- [101] Wasif Husain and Anthony W. Thomas. Novel neutron decay mode inside neutron stars. *Journal of Physics G Nuclear Physics*, 50(1):015202, January 2023. doi:10.1088/1361-6471/aca1d5.
- [102] Julio F. Navarro, Carlos S. Frenk, and Simon D. M. White. The Structure of Cold Dark Matter Halos. *Astrophys. J.*, 462:563, May 1996. doi:10.1086/177173.
- [103] Hai-Nan Lin and Xin Li. The dark matter profiles in the Milky Way. *Monthly Notices of the RAS*, 487(4):5679–5684, August 2019. doi:10.1093/mnras/stz1698.
- [104] Yoshiaki Sofue. Rotation Curve and Mass Distribution in the Galactic Center - From Black Hole to Entire Galaxy. *Publications of Astronomical Society of Japan*, 65:118, December 2013. doi:10.1093/pasj/65.6.118.
- [105] K. Strobel, Ch. Schaab, and M. K. Weigel. Proper-

- ties of non-rotating and rapidly rotating protoneutron stars. *Astronomy and Astrophysics*, 350:497–512, October 1999. doi:10.48550/arXiv.astro-ph/9908132.
- [106] David Radice, Adam Burrows, David Vartanyan, M. Aaron Skinner, and Joshua C. Dolence. Electron-capture and Low-mass Iron-core-collapse Supernovae: New Neutrino-radiation-hydrodynamics Simulations. *Astrophys. J.*, 850(1):43, November 2017. doi:10.3847/1538-4357/aa92c5.
- [107] Yudai Suwa, Takashi Yoshida, Masaru Shibata, Hideyuki Umeda, and Koh Takahashi. On the minimum mass of neutron stars. *MNRAS*, 481(3):3305–3312, 09 2018. ISSN 0035-8711. doi:10.1093/mnras/sty2460.
- [108] Victor Doroshenko, Valery Suleimanov, Gerd Pühlhofer, and Andrea Santangelo. A strangely light neutron star within a supernova remnant. *Nature Astronomy*, 6: 1444–1451, December 2022. doi:10.1038/s41550-022-01800-1.
- [109] J. A. J. Alford and J. P. Halpern. Do Central Compact Objects have Carbon Atmospheres? *Astrophys. J.*, 944 (1):36, February 2023. doi:10.3847/1538-4357/acaf55.
- [110] Afonso Ávila, Edoardo Giangrandi, Violetta Sagun, Oleksii Ivanytskyi, and Constança Providência. Rapid neutron star cooling triggered by dark matter. *Monthly Notices of the RAS*, 528(4):6319–6328, March 2024. doi:10.1093/mnras/stae337.
- [111] Edoardo Giangrandi, Afonso Ávila, Violetta Sagun, Oleksii Ivanytskyi, and Constança Providência. The Impact of Asymmetric Dark Matter on the Thermal Evolution of Nucleonic and Hyperonic Compact Stars. *Particles*, 7(1):179–200, February 2024. doi:10.3390/particles7010010.
- [112] Wasif Husain and Anthony W. Thomas. Possible nature of dark matter. *Journal of Cosmology and Astroparticle Physics*, 2021(10):086, October 2021. doi:10.1088/1475-7516/2021/10/086.
- [113] T. E. Oliphant. Python for scientific computing. *Computing in Science Engineering*, 9(3):10–20, May 2007. ISSN 1521-9615. doi:10.1109/MCSE.2007.58.
- [114] Brian Gough. *GNU Scientific Library Reference Manual - Third Edition*. Network Theory Ltd., 3rd edition, 2009. ISBN 0954612078, 9780954612078.
- [115] S. van der Walt, S. C. Colbert, and G. Varoquaux. The numpy array: A structure for efficient numerical computation. *Computing in Science Engineering*, 13(2):22–30, March 2011. ISSN 1521-9615. doi:10.1109/MCSE.2011.37.
- [116] S. Behnel, R. Bradshaw, C. Citro, L. Dalcin, D. S. Seljebotn, and K. Smith. Cython: The best of both worlds. *Computing in Science Engineering*, 13(2):31–39, March 2011. ISSN 1521-9615. doi:10.1109/MCSE.2010.118.
- [117] Pauli Virtanen, Ralf Gommers, Travis E. Oliphant, Matt Haberland, Tyler Reddy, David Cournapeau, Evgeni Burovski, Pearu Peterson, Warren Weckesser, Jonathan Bright, Stéfan J. van der Walt, Matthew Brett, Joshua Wilson, K. Jarrod Millman, Nikolay Mayorov, Andrew R. J. Nelson, Eric Jones, Robert Kern, Eric Larson, C. J. Carey, İlhan Polat, Yu Feng, Eric W. Moore, Jake VanderPlas, Denis Laxalde, Josef Perktold, Robert Cimrman, Ian Henriksen, E. A. Quintero, Charles R. Harris, Anne M. Archibald, Antônio H. Ribeiro, Fabian Pedregosa, Paul van Mulbregt, and SciPy 1.0 Contributors. SciPy 1.0: fundamental algorithms for scientific computing in Python. *Nature Methods*, 17:261–272, February 2020. doi:10.1038/s41592-019-0686-2.
- [118] Lisandro Dalcín, Rodrigo Paz, Mario Storti, and Jorge D’Elía. Mpi for python: Performance improvements and mpi-2 extensions. *Journal of Parallel and Distributed Computing*, 68(5):655–662, 2008. ISSN 0743-7315. doi:https://doi.org/10.1016/j.jpdc.2007.09.005.
- [119] John D. Hunter. Matplotlib: A 2D Graphics Environment. *Computing in Science and Engineering*, 9(3):90–95, May 2007. doi:10.1109/MCSE.2007.55.
- [120] Thomas Kluyver, Benjamin Ragan-Kelley, Fernando Pérez, Brian Granger, Matthias Bussonnier, Jonathan Frederic, Kyle Kelley, Jessica Hamrick, Jason Grout, Sylvain Corlay, Paul Ivanov, Damián Avila, Safia Abdalla, and Carol Willing. Jupyter notebooks – a publishing format for reproducible computational workflows. In F. Loizides and B. Schmidt, editors, *Positioning and Power in Academic Publishing: Players, Agents and Agendas*, pages 87 – 90. IOS Press, 2016.
- [121] F. Feroz, M. P. Hobson, E. Cameron, and A. N. Pettitt. Importance Nested Sampling and the MultiNest Algorithm. *ArXiv e-prints*, June 2013.
- [122] J. Buchner, A. Georgakakis, K. Nandra, L. Hsu, C. Rangel, M. Brightman, A. Merloni, M. Salvato, J. Donley, and D. Kocevski. X-ray spectral modelling of the AGN obscuring region in the CDFS: Bayesian model selection and catalogue. *Astronomy and Astrophysics*, 564:A125, April 2014. doi:10.1051/0004-6361/201322971.
- [123] Luke Zoltan Kelley. kalepy: a python package for kernel density estimation, sampling and plotting. *Journal of Open Source Software*, 6(57):2784, 2021. doi:10.21105/joss.02784.
- [124] Daniel Foreman-Mackey. corner.py: Scatterplot matrices in python. *The Journal of Open Source Software*, 1 (2):24, jun 2016. doi:10.21105/joss.00024.
- [125] Michael L. Waskom. seaborn: statistical data visualization. *Journal of Open Source Software*, 6(60):3021, 2021. doi:10.21105/joss.03021.
- [126] *Compact stars : nuclear physics, particle physics, and general relativity*, January 2000.
- [127] J. P. W. Diener. Relativistic mean-field theory applied to the study of neutron star properties. *arXiv e-prints*, art. arXiv:0806.0747, June 2008.
- [128] Sean M. Carroll. *Spacetime and geometry. An introduction to general relativity*. Cambridge University Press, Cambridge, 2004. pgs 195,231-233.